INVESTIGATION OF THE TUNABLE NATURE OF RESONANCE WAVELENGTH AND NEAR-FIELD DISTRIBUTION OF PLASMONIC NANOCRESCENTS

by

Cara Michelle Barnes

A thesis submitted to the faculty of
The University of Utah
in partial fulfillment of the requirements for the degree of

Master of Science

Department of Chemistry

The University of Utah

May 2013

The University of Utah Graduate School

STATEMENT OF THESIS APPROVAL

The thesis of **Cara M. Barnes**

has been approved by the following supervisory committee members:

Jennifer Shumaker-Parry	, Chair	**12/14/12** Date Approved
John Conboy	, Member	**12/14/12** Date Approved
Ilya Zharov	, Member	**12/14/12** Date Approved

and by **Henry White** , Chair of the Department of **Chemistry**

and by Donna M. White, Interim Dean of The Graduate School.

ABSTRACT

Plasmonic nanocrescents have been of interest due to their unique optical properties and relative ease of fabrication, as well as their potential applications in surface enhanced spectroscopies. In order to engineer nanocrescents as optimized substrates for these applications, a good understanding of the nanostructure – optical response relationship is necessary. This thesis research focused on understanding the localized surface plasmon resonance (LSPR) wavelength dependence on nanocrescent structural details, such as backbone width, arrayed assemblies, and size. The work presented here shows that the LSPR wavelength can be tuned through a wide spectral region through control of the physical structure of the nanocrescent. This thesis research also focused on understanding the polarization-dependent near-field distribution of the various plasmon resonance modes that arise due to structural asymmetry. The near-field distributions for the short- and long-axis dipoles were mapped through enhanced, localized photopolymerization of photoresist.

TABLE OF CONTENTS

LIST OF FIGURES

LIST OF TABLES

ACKNOWLEDGEMENTS

I am incredibly grateful to everyone who has played a role in making this thesis a possibility. First, I would like to thank my advisor Jennifer Shumaker-Parry, for guiding me through this project while allowing me the freedom to develop into my own scientist. I would also like to thank all of my collaborators, Xiaojin Jiao, Miguel Rodriguez, Rebecca Goldstein, and Steve Blair, without whom this interdisciplinary work would not have been accomplished. I am also indebted to the staff of the SEM and Nanofab facilities, Matt DeLong, Brian Baker, and Brian van Devener, for their constant availability and willingness to assist.

I would also like to thank the Shumaker-Parry group members, both past and present, for laying the foundation of this work and then continuing on with it. Thanks to Cindy Cooper for teaching and training me in the ways of nanocrescents, as well as for all of the fun while in the UK – it was truly a grad school trip of a lifetime. A special thanks to Mark Swartz for making the office a place of both stupidity and intelligence simultaneously – I wholeheartedly enjoyed every laugh and serious conversation.

Finally, to my friends and family – you were such an encouragement through this entire process. There are not enough words to adequately express my thanks. To KB, your support in both science and life has made an immeasurable impact on me. I would not be the person I am today if not for you.

CHAPTER 1

INTRODUCTION

1.1 Localized Surface Plasmon Resonance

Two well-studied size regimes exist in science; the bulk regime of micro-, milli-, and macro-sized materials, and the quantum regime of atoms and molecules. The physical properties of these two size regimes are vastly different from one another. The electrical, mechanical, and optical properties of gold, for example, change as gold is scaled from a single atom to a bulk film. The interface between the two size domains occurs on the nanometer scale and gives rise to unique properties that are not fully quantum or bulk in behavior, but rather a hybrid of the two. This is a consequence of the length scale of the material itself becoming equivalent to the characteristic length of the physical property, thereby altering the behavior of that property.[1] For example, the color that gold appears to the eye is dependent on the size of the gold structure; bulk gold appears to be the well-known golden color, but nanometer sized gold particles can look orange, red, or blue, depending on the particle size.[2] Materials of nanometer dimensions have recently become of interest to scientists and engineers due to the novel properties exhibited in the size regime spanning quantum and bulk dimensions.

One such unique optical property that arises at the nanometer scale is localized surface plasmon resonance (LSPR). LSPR is a physical phenomenon that occurs when electromagnetic radiation of the proper (resonant) wavelength is incident upon metallic structures that are smaller than the wavelength of that light. The incident electromagnetic field induces a coherent oscillation of the free conduction electrons in the metal, which are confined to the metal structure because of the nanoscale dimensions. The induced dipole of the metallic structure creates a local field that is most intense at the metal surface, decaying evanescently into the bulk medium, and is sensitive to local refractive index.[3,4] The LSPR in conjunction with the shape or spatial properties lead to nanomaterials that can act as an antenna to focus the incident light to subwavelength dimensions, leading to enhanced local electric fields.[5] These properties make plasmonic nanostructures an attractive platform for many analytical sensing and spectroscopy applications.

Chemical and biological sensors have been developed utilizing the refractive index sensitivity of the LSPR wavelength of plasmonic nanostructures to detect a wide variety of analytes, such as organophosphorous pesticides[3] and biomarkers for Alzheimer's disease.[4] Bare nanostructures have a specific resonance wavelength that is dependent on the local refractive index of the medium they are in (e.g., air). When molecules, such as self-assembled monolayers, antibodies, or proteins, are attached to the surface of a nanostructure the local refractive index increases and the LSPR wavelength red-shifts. This wavelength shift is related to the thickness and, consequently, the amount of material on the surface. Multilayers of molecules can be built up on the surface of the

nanostructure to create a sensor for a specific target analyte, which can be quantified by measuring the LSPR wavelength shift.

Another major application of plasmonic materials is as substrates for surface-enhanced spectroscopy. When plasmonic nanostructures act as antennas to spatially focus the incident electromagnetic field to subwavelength dimensions, "hot spots" are created and give rise to enhanced signals in a wide variety of spectroscopies. Surface-enhanced Raman scattering (SERS) is the most common enhanced-spectroscopy discussed in literature, where both the incident and Stokes-shifted Raman fields are enhanced.[6,7] Detection of single molecules with SERS has been shown, but enhancement factors of 10^6-10^8 are more commonly reported.[8] Other spectroscopies such as metal enhanced fluorescence (MEF)[9,10] and infrared absorption (SEIRA)[11] also have utilized plasmonic substrates for signal enhancements. In addition to these linear spectroscopies, plasmonic structures also have been shown to enhance nonlinear spectroscopies such as second harmonic generation,[12] two photon fluorescence,[13] and two photon absorption.[14] For both sensing and spectroscopy applications, maximum signal enhancement occurs when the incident excitation wavelength overlaps with the LSPR wavelength of the nanostructure, making structures with tunable LSPR wavelengths widely advantageous.

1.2 Tunability of Plasmonic Nanostructures

The optical properties of plasmonic nanostructures, including the LSPR wavelength, are highly dependent on the physical properties of the structure. As a result, the LSPR wavelength can easily be tuned from the visible to near-infrared region by varying the structural details of the plasmonic material. One of the most straightforward

physical parameters that can be adjusted is the size of the nanostructure, where an increase in the structure size leads to a red-shift in the LSPR wavelength.[15] However, a limit is reached when the particle is no longer smaller than the wavelength of light incident upon it, and propagation of the surface plasmon at the metal-dielectric interface occurs.

Another straightforward physical parameter that can be changed to engineer the resonance wavelength is the metal composition of the nanostructure. All metals that support LSPR are limited in their LSPR wavelengths by their electronic band structure and interband transitions. Gold and silver are the most commonly used metals as they support LSPRs in the visible region with lower limits set by their interband transitions at 516 nm and 326 nm, respectively.[16] Furthermore, gold and silver can be easily modified through thiol chemistry to functionalize surfaces and attach molecules of interest. Other metals in nanoscale dimensions, like copper[17] and aluminum,[18] also can be used as plasmonic materials. Like gold and silver, copper has resonances in the visible region, but with the added benefit of an intense, narrow LSPR wavelength which is advantageous in chemical and biological sensing applications. Aluminum has resonances in the ultraviolet region, making it a unique platform for surface-enhanced spectroscopy applications that utilize UV excitation sources. However, both copper and aluminum form a native oxide layer that significantly affects their resonance wavelengths and fabrication properties, respectively, making them less appealing materials for LSPR applications.

An additional straightforward, tunable property is the geometry of the nanostructure. A myriad of different shapes, including spheres,[19] cubes,[20] pyramids,[21] and stars,[22] can be synthesized and exhibit resonances in the visible region. Synthesized

structures are suspended in solution, and homogeneity can be difficult to achieve when preparing nonspherical particles. One major drawback of these structures is the lack of orientation control, both in solution and when deposited on surfaces. Lithographic techniques provide more control over structure orientation by enabling the fabrication of a variety of nanostructure geometries directly on surfaces. Nanotriangles,[23] disks,[24] and rings[25] all have been fabricated through forms of colloidal lithography and have LSPR wavelengths in the visible region, with the exception of nanorings whose resonance extends into the near-infrared. While there is some control over the nanostructure orientation by fabrication, there is a tradeoff between the time and cost of fabrication and the complexity of the structures that can be made. Lithographic processes that are rapid and allow for the patterning of a large area tend to be limited in the shapes that can be made. Conversely, methods such as electron beam lithography and focused ion beam milling can be used to fabricate any shape, but are serial methods that are time and cost ineffective and can pattern only small areas.

By combining the structural parameters of size, metal, and shape, a plasmonic nanostructure with a specific LSPR wavelength can be engineered and optimized for the specific application at hand. Unfortunately, due to the limitations of these physical parameters, the LSPR wavelength can only be tuned over a small portion of the spectrum (visible to near-infrared), which severely limits the types of spectroscopies that can be enhanced with common nanostructures. There are several potential applications for LSPR that lie just outside of the visible to near-infrared regions of the spectrum, such as surface enhanced infrared absorption (SEIRA) which requires lower energy resonances. Moving resonances into the infrared spectral region is typically difficult even with these tunable

parameters. Other possible applications lie in the ultraviolet (UV) region of the spectrum, such as enhanced fluorescence of biomolecules that are natively weak fluorophores and plasmon-assisted photochemistry. The UV applications require higher energy resonances than are currently available. All of the potential applications outside of the visible to near-infrared regions require novel nanostructures that can be tuned to these spectral regions.

1.3 The Plasmonic Nanocrescent Structure

The nanocrescent is a unique structure that is of interest due to its tunable LSPR wavelength that spans the visible to mid-infrared region.[26-29] When compared to nanotriangles and nanodisks of roughly the same size and metal, nanocrescents exhibit lower energy resonances. Additionally, the tunable physical parameters of nanotriangles and nanodisks are limited to size and metal composition. Through the nanocrescent fabrication process, nanosphere template lithography (NTL), these same parameters plus several additional ones, such as the tip to tip distance and the backbone width, can be controlled.[26] Briefly, NTL involves the deposition of polystyrene or silica nanospheres on a substrate at sub-monolayer coverage with each sphere acting as a template. Metal is deposited at an angle, which leads to metal buildup on one side of the template bead and a shadow on the opposite side. The substrates are etched normal to the surface to remove the metal film that is not masked by the template beads. Once the beads are removed, metal in the shape of crescents is left on the surface.

The structural details, and thus the optical properties, of the fabricated nanocrescents are controlled through various physical parameters during the fabrication

process. The size of the nanocrescent is dictated by the diameter of the template bead, and the composition of the structure is controlled through the choice of metal that is deposited.[27] The structure thickness, backbone width, and tip to tip distance all can be controlled as well to engineer the LSPR to a desired wavelength.

Regardless of the specific structural details of the nanocrescent, the general optical properties are constant, in that multiple resonance modes arise due to the asymmetric nature of the nanocrescent structure. The optical properties are measured with transmission UV-visible-NIR spectroscopy. The uniform size, shape and orientation of nanocrescents on a substrate allow for the probing of the polarization-dependent properties on an ensemble of structures simultaneously. When unpolarized light is incident upon the nanocrescents, four resonance modes are excited simultaneously (Figure 1.1), of which two are of primary interest.[26] An out-of-plane dipole and a quadrupole occur in the visible region, with the quadrupole being lower in energy. The two primary resonance modes of interest are dipolar in nature. One of those is a dipole that arises from charge oscillation between the tips of the nanocrescent and the backbone, and will be referred to as the short axis dipole. This resonance mode typically occurs in the near-infrared region. The second mode of interest is excited by mid-infrared light and occurs due to charge oscillation from one tip of the nanocrescent to the other; this resonance will be referred to as the long axis dipole. These two dipole resonance modes are of interest due to their strong interaction with incident light and have been well-characterized.

Another optical property of interest is the polarization-dependence of the nanocrescent resonance modes due to the asymmetry of the structure. Of the four modes

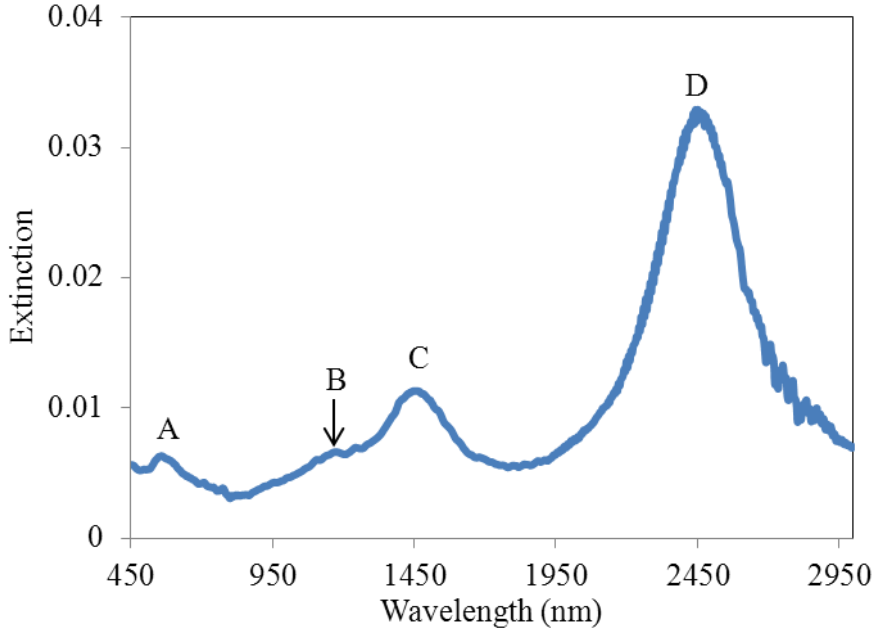

Figure 1.1. Optical properties of gold nanocrescents. Extinction spectrum of the resonance modes of gold nanocrescents excited with unpolarized light. Resonance modes: (A) out of plane dipole; (B) long axis quadrupole; (C) short axis dipole; and (D) long axis dipole.

that arise, three of them can be selectively excited depending on the polarization of the incident light. The out-of-plane resonance is polarization-independent and is excited regardless of the incident polarization. Incident light can either be polarized along the short axis of the crescent or rotated 90° to be along the long axis of the crescent. For light polarized along the short axis of the nanocrescent, the short axis dipole that occurs in the near-IR is selectively excited while the quadrupole and long axis dipole modes are not excited. Similarly, for light polarized along the long axis of the nanocrescent, the quadrupole in the visible region and the long axis dipole in the mid-IR region are selectively excited, while the short axis dipole is not exhibited. Figure 1.2 shows extinction spectra of selectively excited short and long axis resonances, as well as an SEM image of a nanocrescent with the short and long axes defined relative to the structure. The polarization-dependence of plasmonic nanocrescents leads to exciting possibilities as enhancing substrates for various spectroscopies. Not only can the resonance wavelengths be spectrally tuned through structural parameters, the incident light can be polarized to selectively excite resonances in the visible, near-IR and mid-IR. This allows for the possibility of multiple spectroscopies being enhanced from a single nanocrescent substrate by simply changing the polarization and wavelength of incident light.

1.4 The Near-Field of Nanocrescents

In surface-enhanced spectroscopies, maximum signal enhancement occurs when the molecule of interest spatially overlaps with the enhanced near-fields of the plasmonic structure. These enhanced fields are frequently inhomogeneous over the particle surface

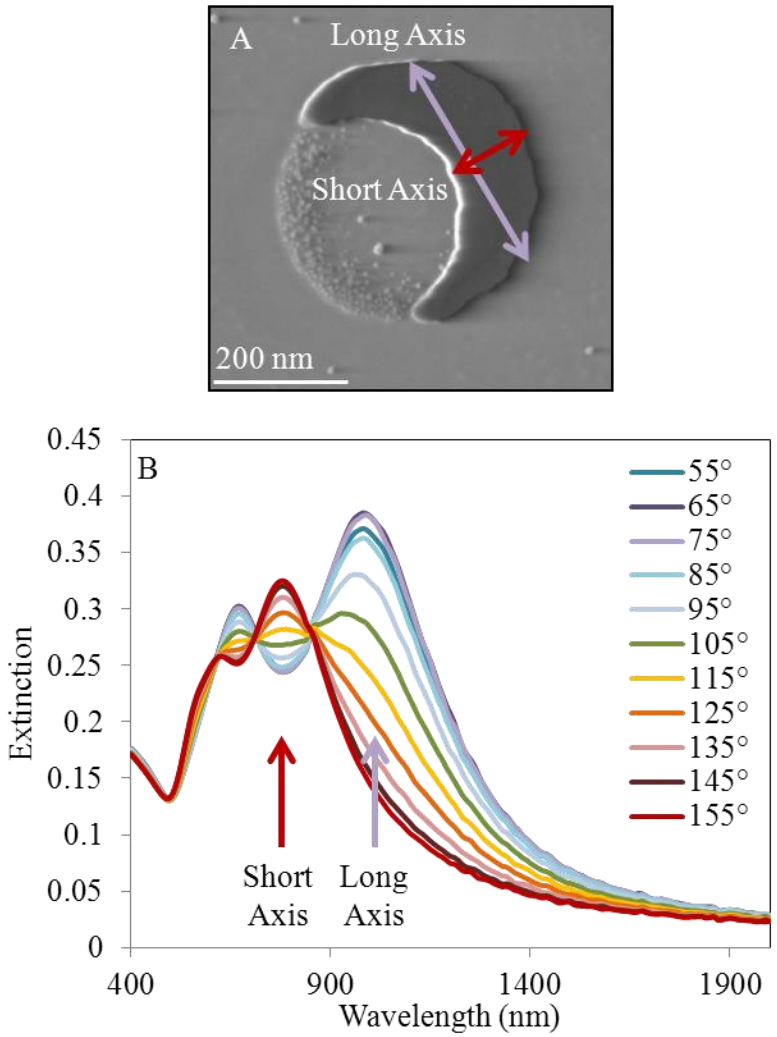

Figure 1.2. Polarization-dependence of optical properties (A) SEM image of gold nanocrescent with short and long axes defined; (B) LSPR spectra of selective excitation of short and long axis dipole resonances. Short axis dipole shown in red and long axis dipole shown in light purple. Polarization angles listed are with respect to the substrate surface. A polarization angle of 155° excites the short axis resonances and a polarization angle of 65° excites the long axis resonances.

and tend to be localized to sharp features such as tips, edges, and gaps.[30-32] Like the LSPR wavelength, the distribution and decay length of the enhanced near-field can be tuned through structural parameters to engineer optimized substrates for a desired application. Surface enhanced spectroscopies are ensemble-based measurements wherein signal is generally obtained over a large area. Molecules that are uniformly adsorbed on a nanostructure experience different near-field enhancements depending on the nonuniform near-field environments that they occupy. Molecules adsorbed in regions of low fields do not necessarily produce any measureable signal; however, due to the non-uniform field environments for the molecules generating signals, there is a non-uniform enhancement per molecule. This makes quantification difficult and reproducibility of signal enhancement a challenge. Understanding and controlling the near-field distribution is necessary for optimizing substrates for surface-enhanced spectroscopies.

Of all of the plasmonic nanostructures reported in the literature, nanocrescents have the highest values for several figures of merit that indicate intense near-fields, and thus show great promise as a substrate for enhanced spectroscopies. Nanocrescents have the highest reported extinction efficiency, a measure of the interaction of light with the plasmonic structure defined as the optical cross section normalized to the geometrical cross section.[27] The nanocrescent also has the highest reported value for refractive index sensitivity, which is the LSPR wavelength shift per refractive index unit, and is a measure of the sensitivity of the resonance.[27] The near-fields of nanocrescents also have been utilized to enhance the molecular vibrations of alkylthiolates in surface-enhanced infrared absorption spectroscopy.[28] The enhancement factor, which is a ratio of the plasmonically-enhanced signal to the nonenhanced signal, is the highest reported area-normalized

SEIRA enhancement factor (46,000) in the literature.[28] The high enhancement factor and high figures of merit indicate intense near-fields of nanocrescents, but do not address the distribution and localization of the fields on the nanocrescent structure, leading to manipulation and control of light on the nanoscale.

In order to understand the distribution and localization of the enhanced near-fields of nanocrescents, finite difference time domain simulations were carried out. These results have shown that when light is polarized along the short axis of the crescent to excite the short axis dipole, the optical near-fields are localized to the tips of the crescent and the outer edge of the backbone. When light is polarized along the long axis of the crescent to excite the long axis dipole, the enhanced near-fields are localized to the tips and extend into the inner diameter of the nanocrescent. While simulations can be informative, it is important to understand the behavior of real structures which have grains and specific structural features that are not included in models. In order to optimize nanocrescents as enhancing substrates, the polarization-dependent near-field distribution must be experimentally determined. Maximized signal enhancement and, thus, better sensitivity could be achieved in surface-enhanced spectroscopies by understanding this near-field localization and subsequently localizing molecules of interest in the regions of highest field enhancement.

1.5 Thesis Overview and Organization

The demand to increase sensitivity in order to detect fewer molecules has led to novel solutions, such as surface-enhanced spectroscopies, which rely on the enhanced near-fields of plasmonic nanostructures. In order to engineer plasmonic substrates for a

desired application, the relationship between the physical properties of the structure and the optical properties must be fully understood. This thesis work investigates the tunable nature of the LSPR wavelength and enhanced near-fields of plasmonic nanocrescents to better design enhancing substrates for spectroscopies.

Chapter 2 describes the tunability of the LSPR wavelength for nanocrescents as structural parameters are varied. Physical parameters that are probed include crescent backbone width and the physical proximity of nanocrescents to each other. Challenges in the fabrication of small nanocrescents are discussed.

Chapter 3 discusses photochemical mapping of the polarization-dependent near-field distribution of nanocrescents through two photon photopolymerization of a photopolymer. Unique near-field distributions were imaged for short and long axis polarization, indicating that the localized near-field of nanocrescents can be tuned for a desired application.

Chapter 4 presents a conclusion to the thesis and summarizes the tunable properties of the LSPR wavelength and near-field distribution of plasmonic nanocrescents. Future studies and possible applications that take advantage of the tunable nature of nanocrescents are discussed.

1.6 References

1. Cademartiri, L.; Ozin, G. A.; Wiley-Vch: Weinheim, 2009; Vol. 1, p 11-49.

2. Mulvaney, P. *MRS Bull.* **2001**, *23*, 1009-1014.

3. Lin, T.-J.; Huang, K.-T.; Liu, C.-Y. *Biosensors and Bioelectronics* **2006**, *22*, 513-518.

4. Haes, A. J.; Chang, L.; Klein, W. L.; Van Duyne, R. V. *JACS* **2005**, *127*, 2264-2271.

5. Talley, C. E.; Jackson, J. B.; Oubre, C.; Grady, N. K.; Hollars, C. W.; Lane, S. M.; Huser, T. R.; Nordlander, P.; Halas, N. J. *Nano. Lett.* **2005**, *5*, 1569-1574.

6. Haynes, C. L.; Van Duyne, R. V. *J. Phys. Chem. B* **2003**, *107*, 7426-7433.

7. Jeanmarie, D.; Van Duyne, R. V. *J. Electroanal. Chem.* **1977**, *84*, 1-20.

8. Willets, K. A.; Van Duyne, R. V. *Annu. Rev. Phys. Chem* **2007**, *58*, 267-297.

9. Ray, K.; Chowdhury, M. H.; Lakowicz, J. R. *Anal. Chem.* **2007**, *79*, 6480-6487.

10. Ray, K.; Szmacinski, H.; Lakowicz, J. R. *Anal. Chem.* **2009**, *81*, 6049-6054.

11. Hartstein, A.; Kirtley, J. R.; Tsang, J. C. *Phys. Rev. Lett.* **1980**, *75*, 201-204.

12. Chen, C. K.; de Castro, A. R. B.; Shen, Y. R. *Phys. Rev. Lett.* **1981**, *46*, 145-148.

13. Kano, H.; Kawata, S. *Opt. Lett.* **1996**, *21*, 1848-1850.

14. Wenseleers, W.; Stellacci, F.; Meyer-Friedrichsen, T.; Mangel, T.; Bauer, C. A.; Pond, S. J. K.; Marder, S. R.; Perry, J. W. *J. Phys. Chem. B* **2002**, *106*, 6853-6863.

15. Kreibig, U.; Genzel, L. *Surf. Sci.* **1985**, *156*, 678-700.

16. Johnson, P. B.; Christy, R. W. *Phys. Rev. B* **1972**, *6*, 4370-4379.

17. Chan, G. H.; Zhao, J.; Hicks, E. M.; Schatz, G. C.; Van Duyne, R. V. *Nano. Lett.* **2007**, *7*, 1947-1952.

18. Langhammer, C.; Schwind, M.; Kasemo, B.; Zoric, I. *Nano. Lett.* **2008**, *8*, 1461-1471.

19. Ghosh, S. K.; Nath, S.; Kundu, S.; Esumi, K.; Pal, T. *J. Phys. Chem. B* **2004**, *108*, 13963-13971.

20. Sun, Y.; Xia, Y. *Science* **2002**, *298*, 2176-2179.

21. Hasan, W.; Stender, C. L.; Lee, M. H.; Nehl, C. L.; Lee, J.; Odom, T. W. *Nano. Lett.* **2009**, *9*, 1555-58.

22. Nehl, C. L.; Liao, H.; Hafner, J. H. *Nano. Lett.* **2006**, *6*, 683-688.

23. Hulteen, J. C.; Treichel, D. A.; Smith, M. T.; Duval, M. L.; Jensen, T. R.; Van Duyne, R. V. *J. Phys. Chem. B* **1999**, *103*, 3854-3863.

24. Hanarp, P.; Kall, M.; Sutherland, D. S. *J. Phys. Chem. B* **2003**, *107*, 5768-5772.

25. Aizpurua, J.; Hanarp, P.; Sutherland, D. S.; Kall, M.; Bryant, G. W.; Garcia de Abajo, F. J. *Phys. Rev. Lett.* **2003**, *90*, 057401.

26. Shumaker-Parry, J. S.; Rochholz, H.; Kreiter, M. *Adv. Mater.* **2005**, *17*, 2131-2134.

27. Bukasov, R.; Shumaker-Parry, J. S. *Nano. Lett.* **2007**, *7*, 113-118.

28. Bukasov, R.; Shumaker-Parry, J. S. *Anal. Chem.* **2009**, *81*, 4531-4535.

29. Bukasov, R.; Ali, T. A.; Nordlander, P.; Shumaker-Parry, J. S. *ACS Nano* **2010**, *4*, 6639-6650.

30. Kottman, J. P.; Martin, O. J. F.; Smith, D. R.; Schultz, S. *Chem. Phys. Lett.* **2001**, *341*.

31. Kottman, J. P.; Martin, O. J. F.; Smith, D. R.; Schultz, S. *Phys. Rev. B* **2001**, *64*, 2325402.

32. Hao, E.; Bailey, R. C.; Schatz, G. C.; Hupp, J. T.; Li, S. *Nano. Lett.* **2004**, *4*, 327-330.

CHAPTER 2

LOCALIZED SURFACE PLASMON RESONANCE WAVELENGTH TUNABILITY THROUGH FABRICATION

2.1 Introduction

Due to the LSPR wavelength and, thus, potential applications being dependent on the physical characteristics of a nanostructure, there is great interest in investigating new methods to produce plasmonic materials. Plasmonic materials can be made either through bottom-up synthesis approaches[1] or top-down fabrication techniques.[2] Bottom-up strategies to produce plasmonic particles rely on synthetic methods where metal salts are reduced to metal atoms that nucleate and grow into particles. The key advantage of this approach is the atomic and molecular scale control over the particles.[3] Bottom-up approaches also tend to be cost effective and easily scaled to produce large quantities of material. Through control of experimental parameters, such as growth time, stabilizing ligands, and reducing agent, the size and shape of the particle can controlled, but only within a limited range. Another challenge of this approach is assembly of the structures into a more complex structure or onto a surface with uniform orientation. The synthesized structures can have a high polydispersity and are difficult to organize, such as in arrayed assemblies with uniform orientation. The structures also must be coated with stabilizing

ligands, which can be difficult to displace with molecules of interest when the nanoparticles are employed for a specific application. Unlike bottom-up synthesis strategies, top-down approaches rely on fabrication techniques such as lithography.[3] While fabrication is disadvantageous in terms of cost, scalability, and the ability to pattern large areas, top-down strategies overcome most of the drawbacks of the bottom-up approach. Plasmonic structures produced through fabrication are on substrates rather than in solution, and can be varied in size, shape, and composition, leading to a wider range of materials. There also is more organizational control over structure orientation and assembly. Top-down approaches are advantageous because they produce bare nanostructures that can be functionalized for a specific application, as opposed to ligand stabilized particles where ligand exchange can be incomplete.

The most commonly used methods for top-down fabrication are lithographic processes such as electron beam lithography (EBL),[4] focused ion beam milling (FIB),[5] and nanosphere template lithography (NTL), an adaptation of nanosphere lithography.[6,7] Both EBL and FIB are patterning techniques that allow for the fabrication of a wide variety of geometries but suffer from being serial processes that are time and cost inefficient for fabricating over large areas or preparing a large number of structures. The structures fabricated from these methods also can be contaminated from photoresist residue (EBL)[8] and ion implantation (FIB).[9] While NTL is limited in the fabricated geometries, the approach can rapidly pattern large substrate areas in parallel. This is of particular interest for producing surface enhanced spectroscopy substrates. Fabrication by NTL creates reproducible, uniformly oriented structures on a surface with several handles for tuning nanostructure optical properties.[6,10] Physical parameters, such as composition

and size, can easily be adjusted to tune the LSPR wavelength of the fabricated nanostructures. In the work presented here, gold nanocrescents were fabricated by NTL and various structural details, such as backbone width and organization of structures into arrays, were adjusted. The optical properties of these nanocrescents were then characterized to understand the effect of these structural details on LSPR wavelength.

2.2 Experimental

Au pellets (99.999%) were purchased from K. J. Lesker (Philadelphia, PA). Polybead Polystyrene Microspheres (505±8 nm and 82±6 nm in diameter) and Silica Microspheres (100±30 nm) were obtained from Polysciences, Inc. (Warrington, PA). Glass microscope slides were purchased from Ted Pella (Redding, CA). A NANOpure Diamond system from Barnstead was used to purify all water used in substrate preparation to 18 MΩ-cm. Absolute ethanol (200 proof) was purchased from Aaper (Shelbyville, KY).

Glass microscope slides were used as substrates and were cleaned by immersing the slides in freshly prepared piranha solution (3:1 volume ratio of H_2SO_4: 30% H_2O_2) for 45 minutes. Slides were then rinsed three times with NANOpure water followed by sonication in 5:1:1 volume ratio H_2O:NH_4OH:30% H_2O_2 at 60°C for 1 h. Slides were again rinsed three times with NANOpure water and either stored in NANOpure water for up to one week or rinsed with absolute ethanol and used immediately.

Nanosphere template lithography was used to fabricate both isolated and arrayed nanocrescents and is shown schematically in Figure 2.1.[6] Template preparation is the first

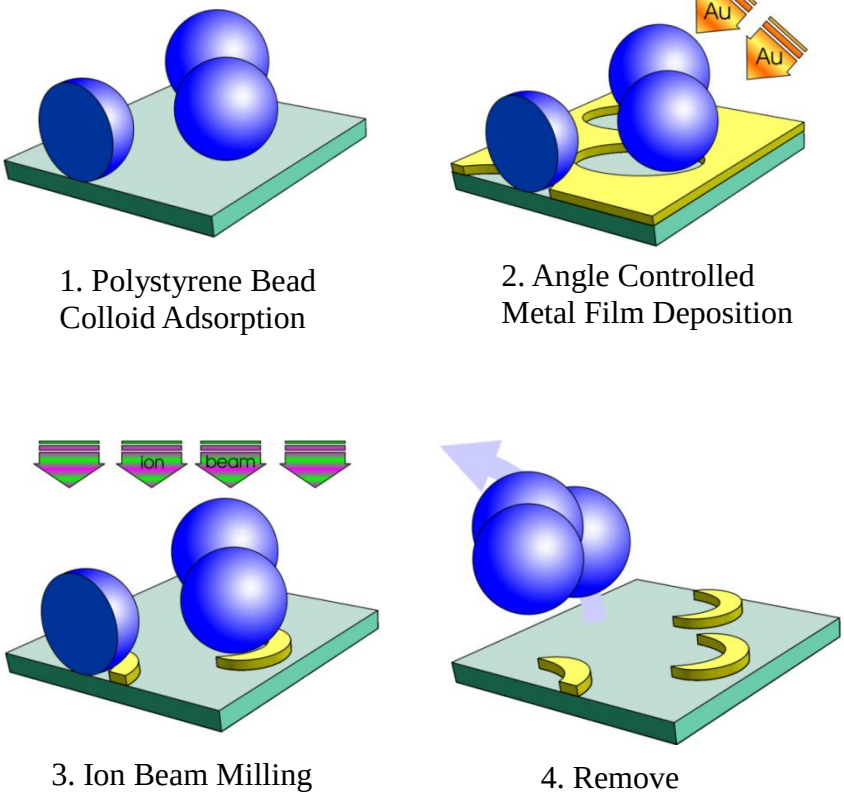

1. Polystyrene Bead Colloid Adsorption

2. Angle Controlled Metal Film Deposition

3. Ion Beam Milling

4. Remove

Figure 2.1. Schematic of nanosphere template lithography. Adapted from reference 6.

step of NTL and is the only step that varies in the fabrication of isolated nanocrescents or arrays of nanocrescents. For both types of templates, the concentrated nanosphere solution was sonicated for 10-15 min at room temperature and then diluted. For isolated nanocrescents, the template was either polystyrene nanospheres diluted 1:20 in absolute ethanol or silica nanospheres diluted 1:40 in absolute ethanol. Isolated nanocrescent templates were fabricated by spin coating a 10 µL aliquot of either the diluted polystyrene or silica nanospheres onto clean glass substrates to form sub-monolayer coverage. For array templates, only polystyrene nanospheres were used, and the beads were diluted 1:5 in 50% absolute ethanol and 50% nanopure water. Array templates were prepared by drop casting a 10 µL aliquot of the diluted polystyrene nanosphere solution onto clean glass substrates and allowing the solution to dry by evaporation in ambient conditions. Under these solution and drying conditions, a hexagonal close-packed monolayer of beads is formed on the surface of the substrate. Exposure of the close-packed template to an oxygen plasma for 120 seconds resulted in the template beads being reduced in diameter while maintaining their lateral position. Once the template has been deposited, the following fabrication steps of NTL are the same for both isolated nanocrescents and arrays of nanocrescents.

After template deposition, a thin metal film is deposited at an angle using an electron beam evaporator (Denton Vacuum USA, Moorestown, NJ). A quartz crystal microbalance (XPC2, Inficon, East Syracuse, NY) was used to measure the film thickness (20-50 nm) and deposition rate (1.0 Å/s). Angled metal deposition leads to a shadow on one side of the bead and metal build up on the other side. The samples were then etched by argon plasma (Plasmalab 80 Plus, Oxford Instruments, Witney, Oxon,

UK) normal to the surface to remove the continuous metal film not protected by the template beads. Metal that is masked by the template bead is not removed. Nanosphere templates are lifted off via the application of tape.

Other nanostructures can be fabricated with variations of nanosphere template lithography, such as nanodisks and nanorings. Figure 2.2 shows a schematic of the fabrication process of these two types of nanostructures. Briefly, nanodisks are fabricated by depositing a metal film on a substrate and then depositing the nanosphere template on the metal film. The remainder of the fabrication steps are the same as for nanocrescent fabrication. Nanorings are fabricated by depositing a nanosphere template onto a substrate and then depositing metal normal to the surface, rather than at an angle, as for nanocrescents.

The optical properties of the nanocrescents were characterized with transmission UV/VIS/NIR spectroscopy (Lambda 9, Perkin Elmer, Waltham, MA) equipped with a polarizer accessory. Extinction spectra were measured over a wavelength range of 400 – 3200 nm with incident light polarized either along the short axis or long axis of the nanocrescent. The structural properties of the nanocrescents were characterized with scanning electron microscopy (Nova NanoSEM 630, FEI, Hillsboro, OR) equipped with a Helix detector. ImageJ software was used to analyze SEM images.

2.3 LSPR Tunability via Nanocrescent Backbone Width

Common planar nanostructures like triangles and disks provide only a few physical parameters that can be controlled to tune the plasmon resonance wavelength of the structures.[11,12] Structure height, diameter, and metal are the most straightforward

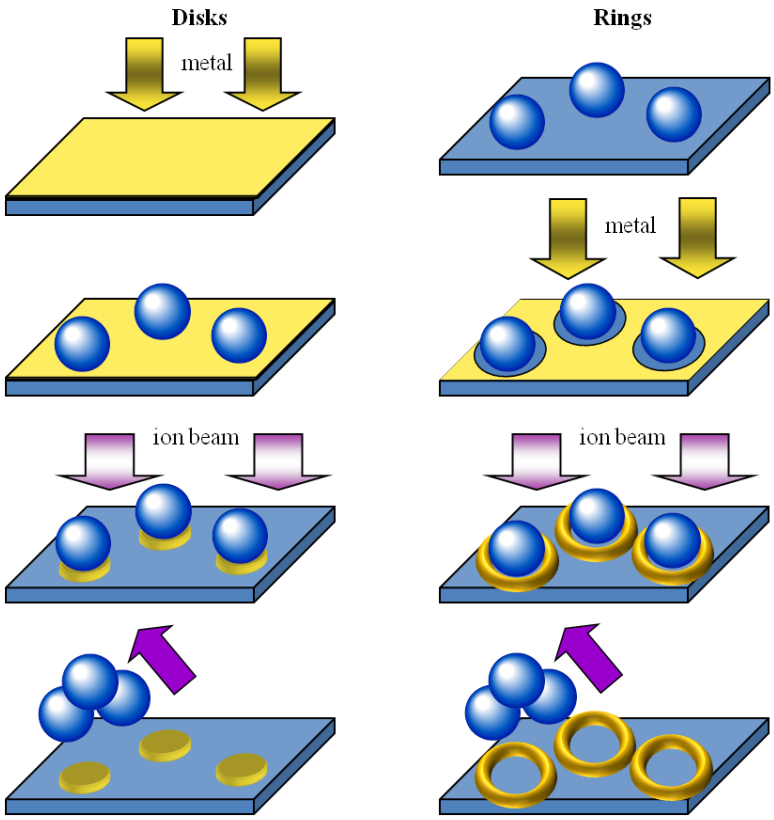

Figure 2.2. Fabrication of nanodisks and nanorings. Schematic of nanodisks and nanorings fabrication through variations in nanosphere template lithography.

of these, but only allow access to a narrow spectral range. Conversely, nanocrescents are plasmonic structures that offer LSPR tunability through a wider spectral range as their unique structure can be controlled through several additional physical parameters.[6,10]

One such parameter is the nanocrescent backbone width, which is controlled by the metal deposition angle which is defined relative to the surface normal.[6] As the metal deposition angle increases, the incident metal accumulates across a larger area under the template bead and generates a wider nanocrescent backbone. Initial studies performed by Kreiter[13] and Bukasov[14] show that the LSPR wavelength blue shifts with increasing backbone width; however, no systematic study has been performed to correlate nanocrescent LSPR wavelength to backbone width. In order to systematically probe the effect of backbone width on LSPR wavelength here, gold nanocrescent arrays were fabricated with varying metal deposition angles.

In this study 505 nm polystyrene beads were used as the template and were exposed to O_2 plasma for 120 seconds, resulting in a template that was 395 ± 30 nm. NTL was then performed following standard procedures with gold deposition angles of 20°, 40°, and 60°. The electron beam evaporator used in this study to deposit metal has a fixed position for the metal crucible. Consequently, the metal deposition angle was controlled by positioning the template-coated substrates upside down on triangular mounts of varying angles. The resulting nanocrescent structures, shown in Figure 2.3, have equivalent height and diameter and varied solely in backbone width. Table 2.1 summarizes the physical parameters of these nanocrescents. It should be noted that the structures fabricated with a metal deposition angle of 60° have a notch in the outer edge

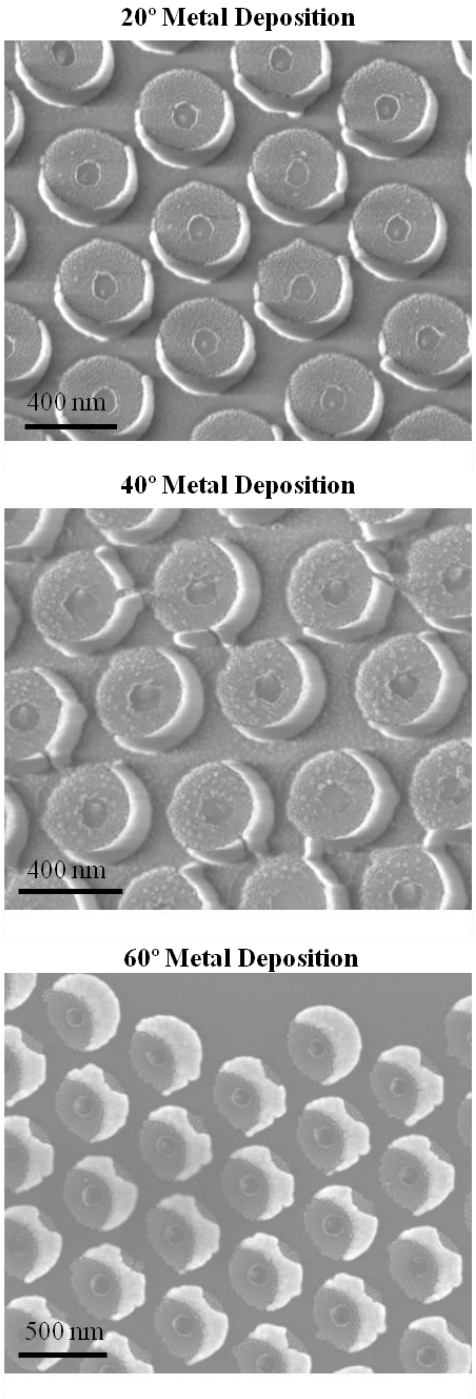

Figure 2.3. SEM images of nanocrescents with increasing backbone widths due to fabrication with increasing metal deposition angles.

Table 2.1. Structural details of nanocrescents fabricated at varying deposition angles. The error reported is the standard deviation of at least 25 data points.

Deposition Angle	**Nominal Metal Thickness (nm)**	**Crescent Diameter (nm)**	**Backbone Width (nm)**
20°	45.0	445 ± 6	76 ± 6
40°	45.1	445 ± 9	100 ± 5
60°	45.2	448 ± 1	162 ± 3

of the backbone. This is due to the spacing between the template beads not being large enough to accommodate the full width of the metal deposited, and neighboring beads shadowed areas where metal should have been deposited.

Optical characterization of these nanocrescent samples are shown in Figure 2.4. Figure 2.4A shows that the short axis dipole plasmon resonance blue shifts for nanocrescents with increasing backbone width. Similarly, in Figure 2.4B, both the long axis dipole and long axis quadrupole show a blue shift in the resonance with increasing backbone width. These results are in agreement with the behavior observed by Kreiter[13] and Bukasov.[14] Figure 2.4C shows the plasmon resonance wavelength for all three modes plotted as function of metal deposition angle in order to understand the relationship between LSPR wavelength and backbone width. Although there is a clear blue shift with increasing deposition angle, there does not appear to be a linear trend. This may be due to the notch in the backbones for structures fabricated at 60° as the plasmon resonance wavelength is highly sensitive to physical structure. The notched structures are sufficiently different from the ideal structure to alter the resulting plasmon resonance wavelength. The theory of observing higher energy resonances with increased backbone width is further supported by the fact that the notched structures are less blue shifted than expected. This is consistent with the notch making the overall backbone narrower. Although further study is needed to fully ascertain the plasmon resonance dependence on backbone width, the plot shown in Figure 2.4C could be used to determine what metal deposition angle should be used during fabrication to engineer nanocrescents to exhibit a specific plasmon resonance wavelength.

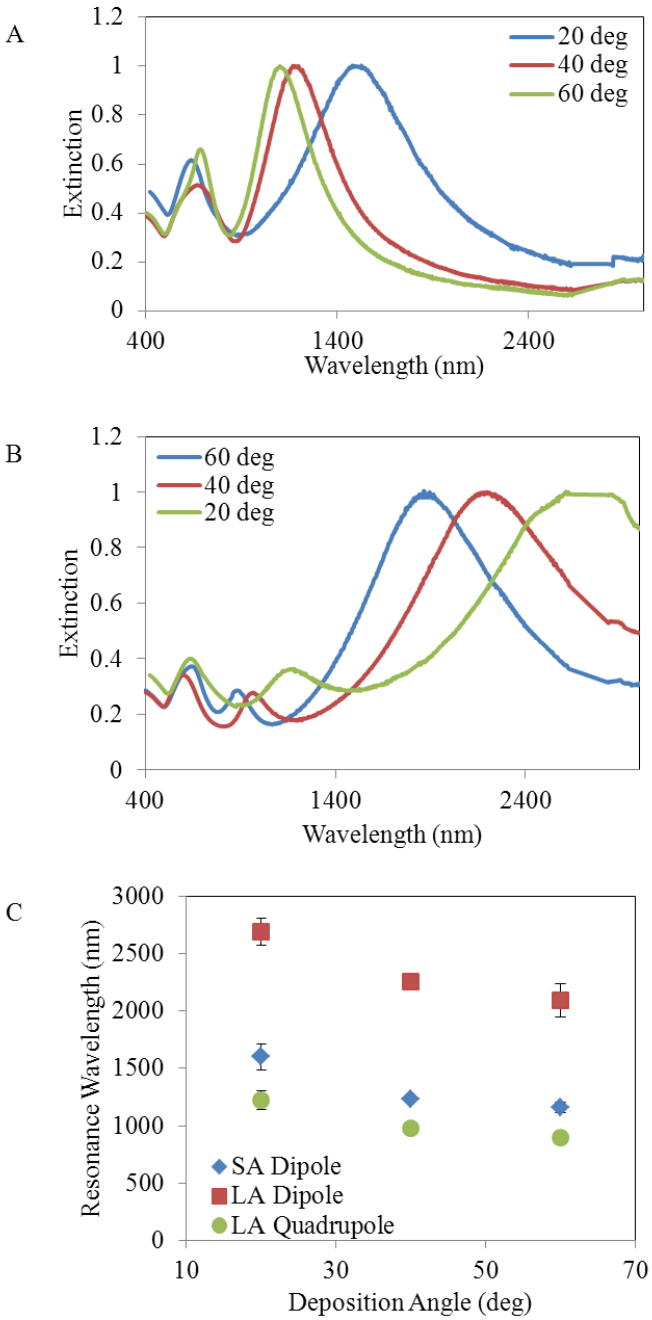

Figure 2.4. Extinction spectra of nanocrescents with increasing backbone widths (A) LSPR spectra of the short axis dipole of nanocrescents fabricated with varying metal deposition angles; (B) LSPR spectra of the long axis dipole and quadrupole of nanocrescents fabricated with varying deposition angles; (C) Plot of plasmon resonance wavelength as a function of deposition angle.

2.4 LSPR Tunability via Coupling in Arrays

Another physical parameter that can be used to tune the plasmon resonance wavelength of a nanostructure is its proximity to other nanostructures. Specifically, the near-fields of isolated nanostructures do not interact with those of adjacent structures; however, increased physical proximity makes this possible in arrays of nanostructures. This leads to coupling of the localized plasmons when structures are in an array, which affects the observed LSPR wavelength and near-field distribution of the structures. Nanocrescent arrays previously have been fabricated,[15,16] but no comprehensive study has been performed to fully understand the effect of coupling on the plasmon resonance tunability. In order to understand the coupling and corresponding effects on the LSPR tunability, nanocrescent arrays were compared to dispersed nanocrescents with no expected coupling of the plasmon resonances. Nanocrescent arrays were fabricated as described in the Experimental section.

In comparing arrays to isolated nanocrescents, multiple variables were considered. First, the effect of the shrunken nanosphere template was investigated. During the polystyrene shrinking process, the initially spherical bead does not maintain its shape.[16] As the bead is exposed to O_2 plasma, the top part of the bead experiences the plasma, while the bottom part of the bead in contact with the substrate is protected. This results in the top part of the bead being etched and flattened, so that the final polystyrene template that is used to fabricate nanocrescents is no longer perfectly spherical. Since nanocrescent arrays can only be fabricated with shrunken templates, the effect of shrinking the template was investigated by comparing the arrays to two types of isolated nanocrescents. The first type, denoted isolated and not shrunken, was fabricated by spin

coating 356 nm polystyrene beads onto a substrate to create a sub-monolayer of the template. The second type, denoted isolated and shrunken, was fabricated by spin coating 505 nm polystyrene beads to form a sub-monolayer. The template was then exposed to anO_2 plasma for 120 seconds, resulting in a template that was approximately 395 nm in diameter. Both types of isolated templates were used to fabricate nanocrescents following standard NTL procedures.

The physical and structural details of the three types of nanocrescents, along with their plasmon resonance wavelengths, are summarized in Table 2.2. While all three types of nanocrescents had the same diameter, the backbone width of the nanocrescent arrays was significantly narrower than the isolated structures. The source of this discrepancy is unclear as all three types of nanocrescents were fabricated with a metal deposition angle of 40°. This should have resulted in comparable backbone widths for all structures. Figure 2.5A and B show the optical response of the three types of structures when light is polarized along the short axis and long axis of the nanocrescents, respectively. From Figure 2.5A, it is clear that the nanocrescent array exhibits red-shifted plasmon resonances relative to the isolated, shrunken crescents, but unmoved relative to the isolated, not shrunken crescents. A similar LSPR red-shift of the array compared to the isolated shrunken crescents can be seen in the long axis spectra in Figure 2.5B. It is interesting to note that the two types of isolated structures, while having the same diameter and backbone width do not have the same LSPR wavelength in both the short and long axes polarizations. It is unclear why this shift in resonance occurs. Additionally, the LSPRs of the array red-shift compared to the isolated, not shrunken crescents.

Table 2.2. Structural details and optical properties of different types of nanocrescents. Error reported for structural parameters is the standard deviation of at least 25 data points and the error reported for plasmon resonance wavelengths is the standard deviation of at least 5 data points.

Crescent Type	**Template Diameter (nm)**	**Crescent Diameter (nm)**	**Backbone Width (nm)**	**Short Axis Resonance (nm)**	**Long Axis Resonance (nm)**
Isolated, shrunken	395	443 ± 12	174 ± 10	1134 ± 27	1979 ± 86
Isolated, not shrunken	356	444 ± 9	162 ± 3	1249 ± 40	2147 ± 88
Array, shrunken	395	445 ± 9	100 ± 5	1235 ± 18	2251 ± 45

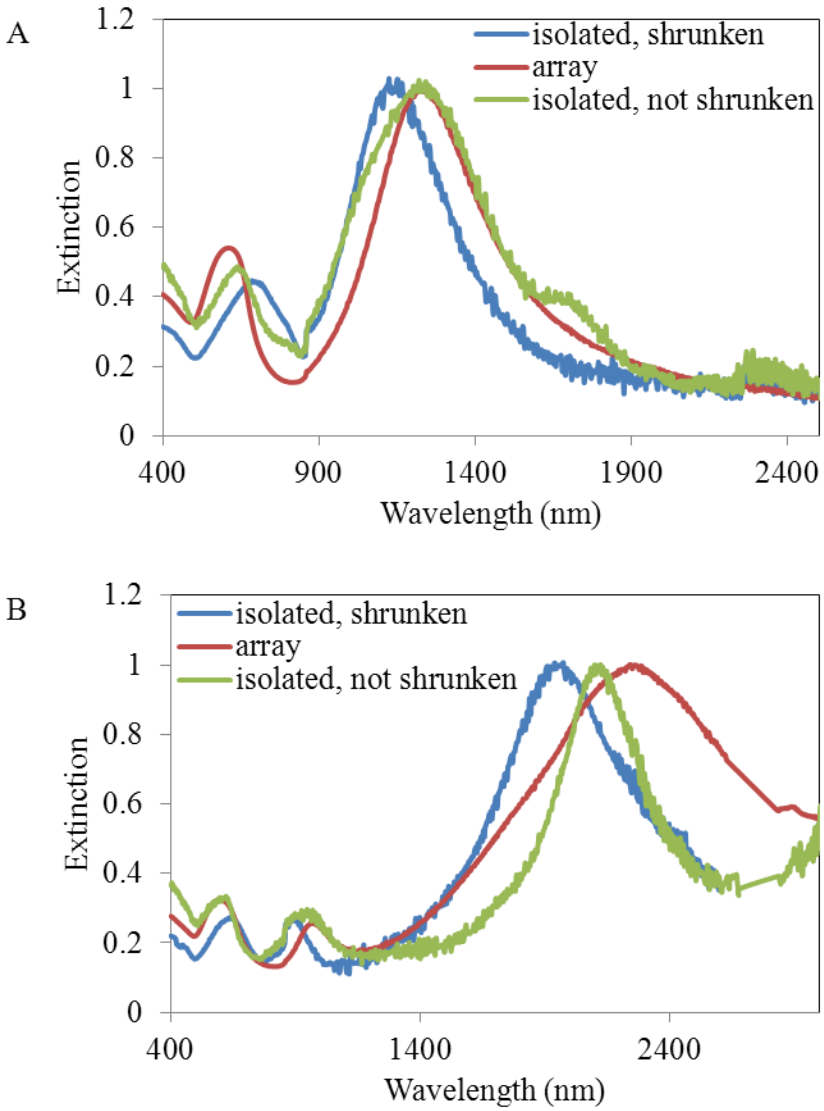

Figure 2.5. Extinction spectra of isolated and arrayed nanocrescents. LSPR spectra of the short axis dipole of isolated and arrayed nanocrescents (A) and LSPR spectra of the long axis dipole of nanocrescents (B).

No conclusions can be drawn yet about the plasmon resonance wavelength tunability due to coupling in arrays because it is likely that the red-shifted resonance of arrays is due to the interplay of several factors that were unaccounted for. It is possible that the arrays have a lower energy resonance due to plasmon coupling between neighboring structures, but it also could be due to the difference in backbone width, thickness, tip sharpness or orientation in arrays. These factors have not undergone systematic investigation, so their impact cannot be isolated. One great asset of NTL and the nanocrescent structure is the multiple degrees of freedom in the structure, but this also means understanding the structure – optical response relationship with each degree of freedom in isolation is challenging. Studies are ongoing in by the Shumaker-Parry group to further understand nanocrescent behavior in arrays.

2.5 Challenges of LSPR Tunability in the Near-Infrared

As has been previously demonstrated, the LSPR wavelength of nanocrescents can be tuned over a relatively wide wavelength range by varying the diameter of the structure. Nanocrescents exhibiting lower energy, infrared plasmons have been studied more extensively than higher energy nanocrescents due to their potential applications in surface-enhanced infrared absorption and their relative ease in fabrication.[10,17] However, less is understood about the material properties and optical responses of visible to near-infrared (NIR) resonant nanocrescents. Scaling nanocrescents down to have visible or NIR resonances has potential applications in surface-enhanced Raman scattering[18] or multiphoton processes such as second harmonic generation[19] or two-photon absorption.[20]

In order to tune the LSPR wavelength of nanocrescents to the visible or NIR, the structures themselves must be sub-150 nm in diameter, which necessitates the use of a template that is 100 nm or less in diameter.[10] Figure 2.6A shows the LSPR spectra for a nanocrescent sample fabricated using dispersed 82 nm polystyrene beads as a template. The short axis dipole is resonant in the visible region at 685 nm, the long axis dipole is resonant in the NIR at 900 nm, and additional modes such as the out of plane dipole and long axis quadrupole are resonant in the visible region. However, scanning electron microscopy (SEM) images (Figure 2.6B) revealed that the tips of the nanocrescents were connected either with metal that was re-deposited during the etching process or with polystyrene residue. The material spanning the tips could not be removed with tape, UV-ozone cleaning, various solvents or sonication.

In order to determine the composition of the material spanning the tips, the etching process during fabrication was investigated. Samples were fabricated with 82 nm polystyrene template beads dispersed in submonolayer coverage followed by gold deposition at 40°. Samples were then etched for times ranging from 3 – 17 min and imaged with SEM. Figure 2.7 shows SEM images of samples at various times during the etching process. The spherical polystyrene bead capped with gold, along with the shadow cast by the bead can be seen in the initial image of an unetched sample. Between 6 and 8 min, the polystyrene beads begin to deform at the bead center. It appears that the polymeric material is pushed radially from the center of the bead and builds up on the inner edge of the crescents and between the two tips. During this range of etching times, the gold film is no longer continuous, but rather islands are present on the surface as the metal begins to be etched away. At longer etching times of 13 – 17 min, the polystyrene

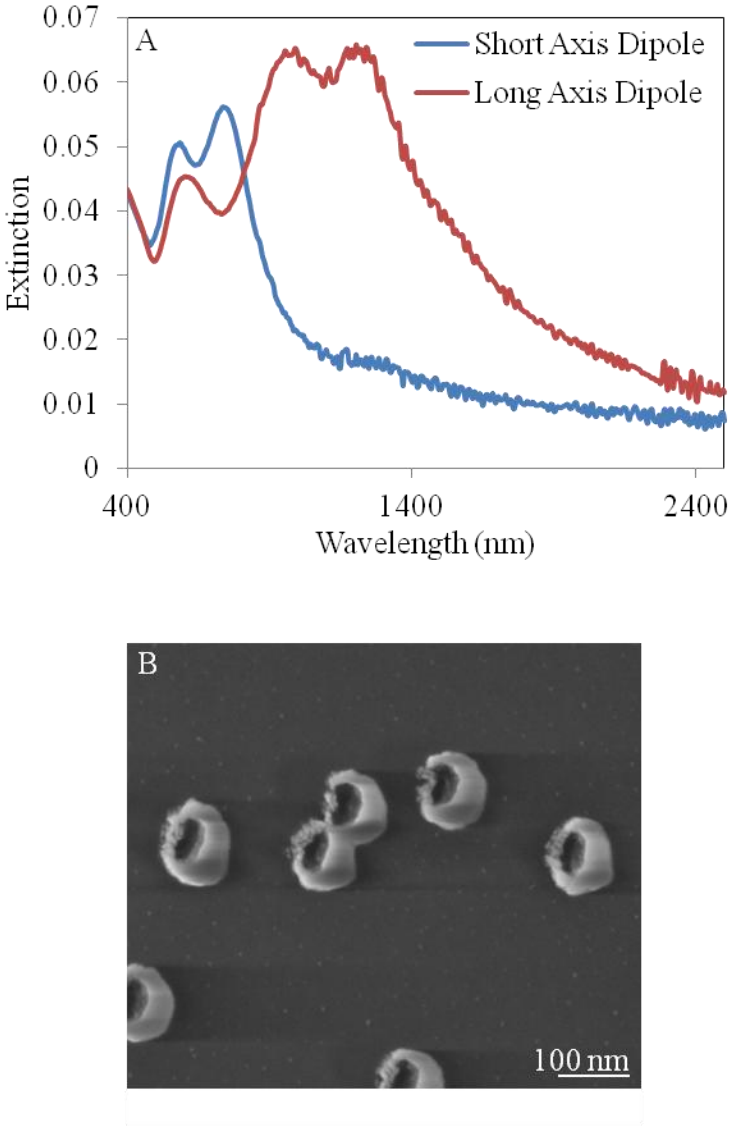

Figure 2.6. Characterization of nanocrescents fabricated with polystyrene templates. LSPR spectra (A) and SEM image (B) of gold nanocrescents fabricated with a polystyrene nanosphere template.

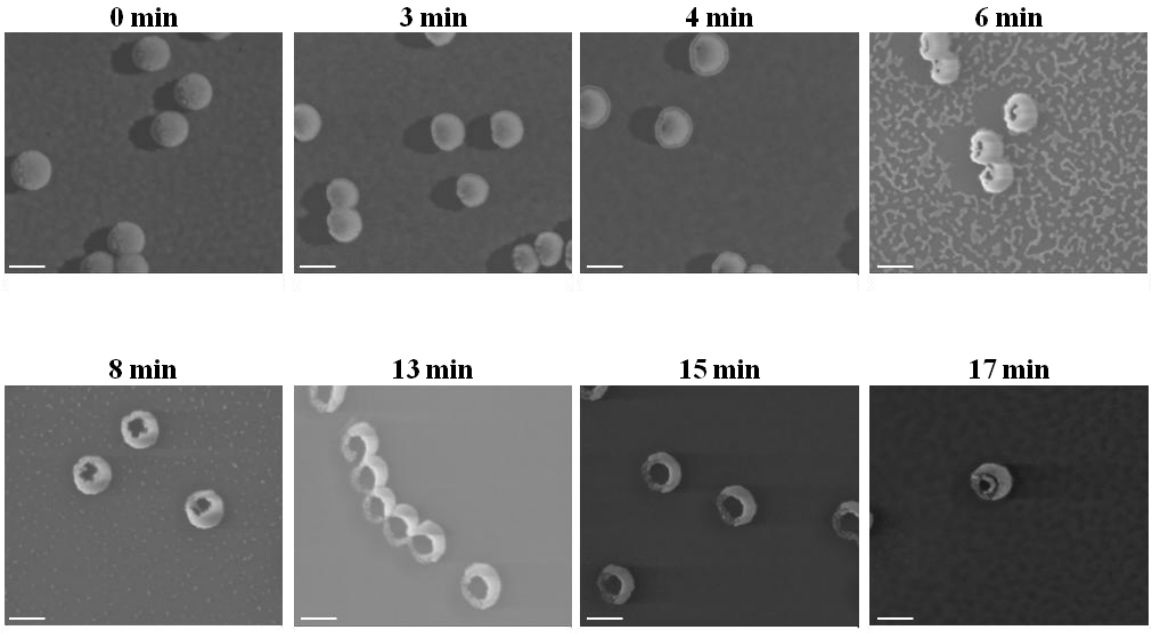

Figure 2.7. SEM images of etching step of fabrication process. Melting of polystyrene nanosphere template during the etching process of nanocrescent fabrication. All scale bars are 100 nm.

residue between the tips and on the inner edge of the crescents is further etched. Unfortunately, as the polystyrene bead is etched it no longer acts as a mask to protect the underlying gold crescent. Longer etch times (approximately 17 min) begin to remove not only the polystyrene residue, but the nanocrescents as well. It is thought that the polystyrene beads melt during etching due to a lower melting temperature in this small size regime.[21] This is consistent with our observations and indicates that the residue between the nanocrescent tips is polystyrene.

Silica nanospheres are another template option for the fabrication of nanocrescents and have the benefit of being hard spheres that do not melt or lose their shape during etching. Figure 2.8 shows the LSPR spectra and SEM image of a nanocrescent sample fabricated with 100 nm silica beads as the template. The spectra show that the short axis dipole resonates at 860 nm and the long axis dipole at 1285 nm, both in the NIR region of the spectrum. While silica templates do not melt, they pose a fabrication challenge in that often times they cannot be removed from the substrate without simultaneously removing the nanocrescents. Several methods of bead removal (tape, solvent, sonication) and substrate surface chemistry (polyelectrolyte layers, silanization) were attempted, but either resulted in the beads not being removed or the beads and crescents being removed. The nanocrescent sample shown in Figure 2.8 is an exception in that most of the silica beads have been removed while leaving behind intact nanocrescents. Silica templates give ideal nanocrescent structures with no residue between the tips, but there is not a reproducible method to remove the template.

There have been challenges in the fabrication of nanocrescents with visible and NIR resonances due to the necessary nanostructure dimensions. However, few successes

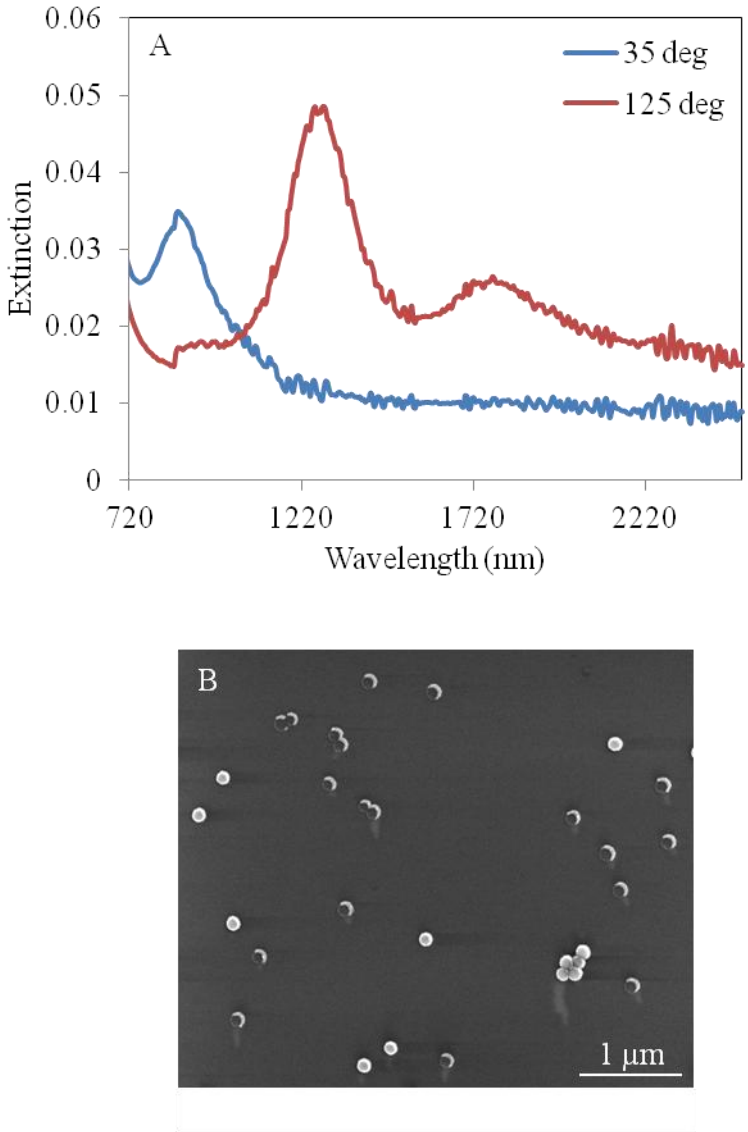

Figure 2.8. Characterization of nanocrescents fabricated with silica templates. LSPR spectra (A) and SEM image (B) of gold nanocrescents fabricated with silica nanosphere templates. Angle of 35° corresponds to polarization along the short axis of the nanocrescents; angle of 125° corresponds to polarization along the long axis of the nanocrescents.

in the fabrication of nanocrescents that access this spectral range have been shown in spite of the limitations of the template materials. Further work could pursue the development of new template materials or other methods to fabricate small nanocrescents in order to tune the plasmon resonance wavelength to higher energies.

2.6 Conclusion

Understanding the relationship between the physical structure and plasmon resonance wavelength is of great interest for applications which require engineering the structures to exhibit a specific plasmon resonance. The work presented here has shown several structural details that can be used to tune the resonance wavelength of plasmonic nanocrescents. First, the width of the nanocrescent backbone was explored. It was found that as the width increases, the short axis dipole and long axis dipole and quadrupole resonances blue-shift. This structural parameter could be used when attempting to engineer high energy resonances for applications in the visible and NIR spectral regions. Secondly, the tunability of nanocrescent resonances in arrays was investigated to determine the effect of interparticle coupling on the resonance wavelength. Initial studies were inconclusive due to the myriad of physical details that were unaccounted for, but did show clearly that nanocrescents possess multiple degrees of freedom in tuning the resonance wavelength. The final structural parameter utilized to tune the resonance wavelength described in this chapter is nanocrescent diameter, with a focus on small structures for visible and NIR applications. It was shown that the fabrication of sub-150 nm nanocrescents is not trivial due to the limitations of the template materials.

2.7 References

1. Wang, Y.; Xia, Y. *Nano. Lett.* **2004**, *4*, 2047-2050.

2. Merkel, T., J.; Herlihy, K. P.; Nunes, J.; Orgel, R. M.; Rolland, J. P.; DeSimone, J. M. *Langmuir* **2010**, *26*, 13086-13096.

3. Cao, G. *Nanostructures and Nanomaterials: Synthesis, Properties, and Applications*; Imperial College Press: London, 2004.

4. Pease, R. F. W. *Contemp Phys* **1981**, *22*, 265-290.

5. Watkins, R. E. J.; Rockett, P.; Thoms, S.; Clampitt, R.; Syms, R. *Vacuum* **1986**, *36*, 961-967.

6. Shumaker-Parry, J. S.; Rochholz, H.; Kreiter, M. *Adv. Mater.* **2005**, *17*, 2131-2134.

7. Hulteen, J. C.; Van Duyne, R. V. *J Vac Sci Technol A* **1995**, *13*, 1553-1558.

8. Chung, S.-W.; Ginger, D. S.; Morales, M. W.; Zhang, Z.; Chandrasekhar, V.; Ratner, M. A.; Mirkin, C. A. *Small* **2005**, *1*, 64-69.

9. Prestigiacomo, M.; Roussel, L.; Houel, A.; Sudraud, P.; Bedu, F.; Tonneau, D.; Safarov, V.; Dallaporta, H. *Microelectron Eng* **2004**, *76*, 175-181.

10. Bukasov, R.; Shumaker-Parry, J. S. *Nano. Lett.* **2007**, *7*, 113-118.

11. Hulteen, J. C.; Treichel, D. A.; Smith, M. T.; Duval, M. L.; Jensen, T. R.; Van Duyne, R. V. *J. Phys. Chem. B* **1999**, *103*, 3854-3863.

12. Hanarp, P.; Kall, M.; Sutherland, D. S. *J. Phys. Chem. B* **2003**, *107*, 5768-5772.

13. Rochholz, H.; Bocchio, N.; Kreiter, M. *New J Phys* **2007**, *9*, 1-18.

14. Bukasov, R.; Ali, T. A.; Nordlander, P.; Shumaker-Parry, J. S. *ACS Nano* **2010**, *4*, 6639-6650.

15. Retsch, M.; Tamm, M.; Bocchio, N.; Horn, N.; Forch, R.; Jonas, U.; Kreiter, M. *Small* **2007**, *5*, 2105-2110.

16. Vogel, N.; Fischer, J.; Mohammadi, R.; Retsch, M.; Butt, H.-J.; Landfester, K.; Weiss, C. K.; Kreiter, M. *Nano. Lett.* **2011**, *11*, 446-454.

17. Bukasov, R.; Shumaker-Parry, J. S. *Anal. Chem.* **2009**, *81*, 4531-4535.

18. Haynes, C. L.; Van Duyne, R. V. *J. Phys. Chem. B* **2003**, *107*, 7426-7433.

19. Chen, C. K.; de Castro, A. R. B.; Shen, Y. R. *Phys. Rev. Lett.* **1981**, *46*, 145-148.

20. Wenseleers, W.; Stellacci, F.; Meyer-Friedrichsen, T.; Mangel, T.; Bauer, C. A.; Pond, S. J. K.; Marder, S. R.; Perry, J. W. *J. Phys. Chem. B* **2002**, *106*, 6853-6863.

21. Williams, R.; Crandall, R. S.; Wojtowicz, P. J. *Phys. Rev. Lett.* **1976**, *37*, 348-351.

CHAPTER 3

PHOTOCHEMICAL MAPPING OF THE POLARIZATION-DEPENDENT NEAR-FIELDS OF PLASMONIC NANOCRESCENTS

3.1 Introduction

Plasmonics, the interaction of light with subwavelength metallic materials, has been a growing area of interest due to the inherent unique optical phenomena that can be exploited.[1-3] Plasmonic nanostructures have the ability to act as optical antennas that focus incident light to subwavelength volumes, leading to potential applications in chemical and biological sensing,[4] photovoltaics,[5] lithography,[6] optical interconnects and waveguides,[7] and near-field microscopy.[8] Another application of plasmonics is in surface-enhanced spectroscopies, such as Raman scattering[9] and fluorescence,[10] to enhance spectroscopic signals and lower detection limits.

All of these applications utilize the localized surface plasmon resonance (LSPR) of metallic nanostructures. This is a physical phenomenon that occurs when incident light perturbs the free conduction electrons of the metal and induces an oscillating dipole that is confined to the subwavelength dimensions of the nanostructure. LSPR gives rise to two main features, the plasmon resonance wavelength and localized, enhanced electromagnetic (EM) fields, both of which can be optimized for maximum performance

in desired applications by controlling physical details of the plasmonic structure, such as size,[11] shape,[12] and composition.[13]

Plasmon excitation results in enhanced EM fields which are typically inhomogeneously distributed around nanostructures and localized to edges, tips, and gaps.[14,15] These features of nanostructures induce an antenna effect to spatially focus incident light into nanoscale dimensions, frequently termed "hot spots."[16] Simulations have shown that for some nanoparticle geometries, enhanced near-fields can exceed the incident field by as many as two or three orders of magnitude.[17] Localized EM fields have been utilized to enhance a myriad of linear and nonlinear spectroscopic processes including Raman scattering[9] and second harmonic generation,[18] as well as one and two photon fluorescence.[10,19] Maximum signal enhancement in any spectroscopic process occurs when the molecule of interest spatially overlaps with the enhanced near-fields of the nanostructure. However, in typical measurements, molecules adsorbed uniformly on nanostructures experience different fields and give rise to nonuniform and unpredictable signals due to the spatial distribution of the near-field. In order to achieve reproducible, maximized enhancement in spectroscopic applications, the near-field behavior of the enhancing nanostructure must be well understood and, ideally, controlled.

Here, we focus on investigating the near-field behavior of the nanocrescent, a plasmonic nanostructure which exhibits tunable plasmon resonances that can be controlled by the incident radiation.[20-24] Due to the asymmetric nature of the nanocrescent structure, different plasmon resonance modes can be selectively excited by controlling the polarization of the incident light. Figure 3.1A is an atomic force microscopy (AFM) image of a nanocrescent with the short and long axes defined relative to the structure

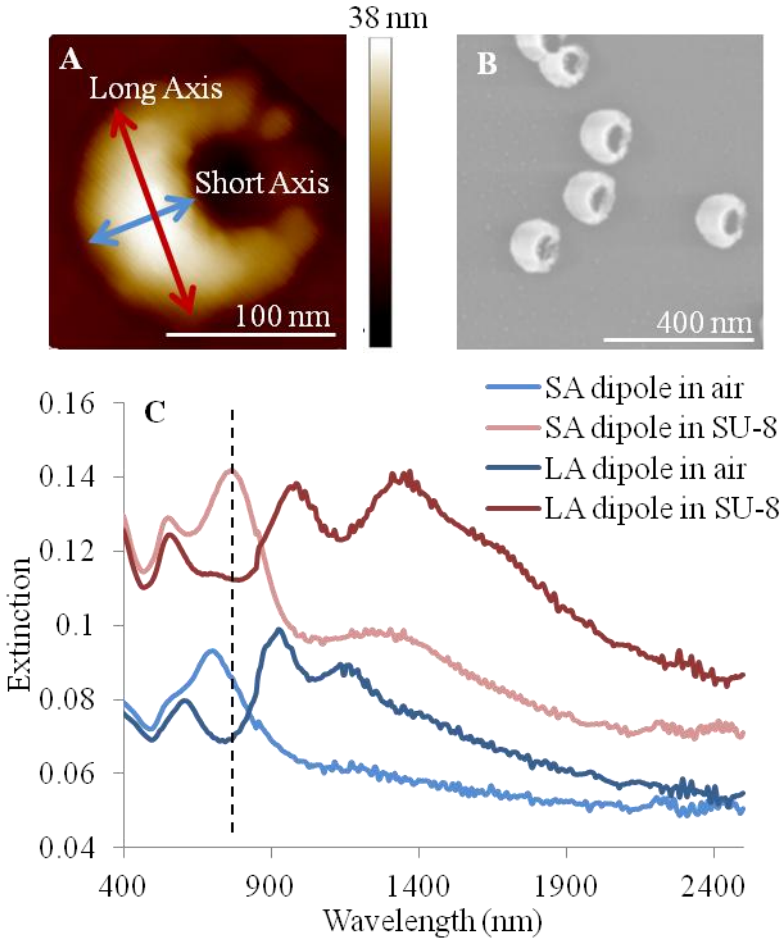

Figure 3.1. Characterization of nanocrescents with plasmon resonances at 800 nm. (A) AFM image and (B) SEM image of bare gold nanocrescents; (C) Polarization-dependent extinction spectra of bare gold nanocrescents and structures covered by a film of SU-8 photoresist; dashed line indicates the wavelength of the Ti:Sapphire laser line used in the photopolymeratization experiments. SA is the short axis and LA is the long axis.

Light polarized along the short axis of the nanocrescent excites a short-axis dipole that corresponds to a charge oscillation between the tips and backbone of the nanocrescent. Light polarized along the long axis of the nanocrescent excites a long-axis dipole corresponding to charge oscillation between the two tips of the crescent and a higher energy quadrupole mode. An out of plane dipole mode also occurs in both short and long axis polarizations. The different charge oscillation patterns of the three plasmon resonance modes impact the observed LSPR wavelengths and are predicted through simulations to lead to different charge confinement and distribution of light in the near-field. Due to the polarization dependence, we expect to be able to tune the spatial distribution of the near-field.

In order to engineer nanocrescents as optimized optical antenna to manipulate light on the nanoscale, it is necessary to first understand the dependence of the near-field distribution on structural details and polarization control. The decay length, location, and distribution of the enhanced EM fields of nanocrescents are all aspects that can be tailored to confine light to subwavelength volumes. Recent interest in nanocrescents as optical antenna has led to them being employed as substrates for surface-enhanced infrared absorption spectroscopy (SEIRA) where the near-fields of silver nanocrescents with plasmon resonances in the infrared were utilized to enhance signals of alkylthiolates.[22] The study found that nanocrescents have the highest area-normalized SEIRA enhancement factor (46,000) reported, indicating intense plasmon-induced near-fields. While this study provided insight to the magnitude of the enhanced EM fields, it was an ensemble measurement providing no information about the location of these intense fields on the nanocrescent.

Another effort to quantify the EM field enhancement on nanocrescents investigated their long-range decay lengths. This was accomplished by sputtering layers of silicon onto the surface of nanocrescents and monitoring the plasmon resonance wavelength shift with increased local dielectric environment.[23] These experiments showed that the decay length of the near-field was approximately 1.5 – 2 orders of magnitude larger than nanotriangles (5 – 15 nm)[25] or rings (12 nm).[26] This study also showed that the decay length could be tuned by varying the diameter and in-plane aspect ratio of the nanocrescent.[23] Again, this study points toward intense optical near-fields for nanocrescents, but used ensemble measurements that cannot resolve the inhomogeneity of the localized EM fields. Thus far, the detailed spatial distribution of the near-field of nanocrescents has not been investigated. Understanding this tunable feature is a vital component to the engineering of optimized substrates for applications utilizing control of subwavelength volumes of light.

In previous efforts to map the near-field distributions of optical antennas, several techniques have been employed. Scanning near-field optical microscopy (NSOM) has been used extensively to map the near-field lateral distribution of nanotriangles,[27] blocks,[28] and nanodisks;[29] however interaction between the NSOM tip and nanostructure near-field leads to convoluted optical responses that are difficult to interpret.[30]

Another method used to probe the near-field distribution is photochemical imaging, which has been demonstrated for a variety of nanostructures including dots,[31] blocks,[32] and bowtie antennas.[33] In this method, the near-fields of the nanostructure enhance light absorption of a photopolymer leading to localized photochemistry that is representative of the location of the near-fields. While linear absorption of photopolymers

has been demonstrated,[31] nonlinear absorption has been utilized more extensively to map near-field distributions.[32-34] Because multi-photon absorption is an inherently weak process, photopolymerization only occurs in regions where the optical near-fields are intense enough to enhance nonlinear absorption; this leads to selective, localized polymerization and higher resolution mapping.[34] The localized photochemistry can then be imaged with conventional techniques, such as scanning electron microscopy (SEM) or atomic force microscopy (AFM), to visualize the near-field location and distribution.

While the photochemically imaged nanostructure results reported in literature have demonstrated the ability to map the near-field distribution through multi-photon absorption of photopolymers, many of the nanostructures studied have had a single polarization-independent plasmon resonance. Also, the previously mapped structures were all fabricated with electron beam lithography, which suffers from being a serial process that is time and cost inefficient when patterning large areas. An advantage of the nanocrescent structure is its structural asymmetry that arises from fabrication via nanosphere template lithography (NTL). NTL employs polymer or silica nanospheres as individual templates for each nanocrescent and allows for parallel patterning of large substrate areas.[20] The versatility of the NTL fabrication process also provides several physical parameters that can be adjusted, such as size, composition, backbone width, and tip-to-tip distance, leading to a plasmon resonance wavelength that is highly tunable from the visible to mid-infrared spectral regions, which in turn leads to tunable near-field patterns.[21] NTL also produces uniformly oriented nanocrescents, which allows for the addressability of an ensemble of structures simultaneously to investigate the polarization dependence of the near-field distributions.

This study was done in collaboration with Xiaojin Jiao, Miguel Rodriguez, Rebecca Goldstein, Mark Swartz, and Steve Blair. In this study, we investigate the near-field distributions of polarization-dependent electromagnetic modes of plasmonic nanocrescents through multiphoton photopolymerization. To probe the near-field patterns, SU-8 photoresist is selectively polymerized through multi-photon absorption in regions of enhanced near-fields. SU-8 has maximum linear absorption at 365 nm wavelength. The locations of photopolymerized SU-8 are visualized with SEM and AFM and the patterns are compared to simulations of the near-field distributions.

3.2 Materials and Methods

Au pellets (99.999%) were purchased from K. J. Lesker (Philadelphia, PA). Polystyrene Microspheres (82 ± 6 nm) were purchased from Polysciences, Inc. (Warrington, PA). SU-8 2000.5 photoresist and developer were purchased from MicroChem Co. (Newton, MA). Glass microscope slides were purchased from Ted Pella (Redding, CA). Absolute ethanol was obtained from Aaper (Shelbyville, KY). All water used for substrate preparation was purified to 18 MΩ with a Barnstead NANOpure Diamond system.

Glass microscope slides were used as substrates and were cleaned by immersion in freshly prepared piranha solution (3:1 volume ratio of H_2SO_4: 30% H_2O_2) for 30 – 45 min. Slides were rinsed three times with nanopure water. Substrates were then sonicated in 5:1:1 volume ratio H_2O: NH_4OH: 30% H_2O_2 at 60 ºC for 1 h, and then rinsed three times with NANOpure water. Substrates were either stored for up to 1 week in NANOpure water or rinsed with absolute ethanol and used immediately.

Gold nanocrescents and nanorings were fabricated on clean glass slides using nanosphere template lithography (NTL). First, polystyrene nanosphere templates were diluted 1:20 volume ratio in absolute ethanol and 10 μL were spin coated onto clean glass slides resulting in submonolayer coverage. Second, a 20 nm gold film was deposited by electron beam evaporation (Denton Vacuum USA, Mooretown, NJ). For nanorings, the metal film was deposited normal to the substrate surface, and for nanocrescents, the metal film was deposited at a controlled angle of 40º relative to the surface normal. Angled metal deposition leads to a shadow being cast on one side of the nanosphere template and metal built up on the other side. A quartz crystal microbalance (XPC2, Inficon, East Syracuse, NY) was used to measure film thickness and deposition rate (1.0 Å/s). The next fabrication step was etching with argon plasma (Plasmalab 80 Plus, Oxford Instruments, Witney, Oxon, UK) normal to the substrate surface to remove the continuous metal film. The metal masked by the template bead is protected. Finally, nanosphere templates were lifted off by the application of tape. Gold nanodisks were fabricated following a similar procedure, except the 20 nm gold film was deposited on clean glass substrates followed by the nanosphere template deposition. The rest of the fabrication procedure was then carried out as described above for crescents and rings.

Nanostructure samples were characterized optically with UV/VIS/NIR transmission spectroscopy (Lambda 9, Perkin Elmer, Waltham, MA) equipped with a polarizer accessory. Extinction spectra were acquired from 400 – 2500 nm with unpolarized light for nanodisks and rings or with the incident electric field polarized either along the short axis or the long axis of the nanocrescents. Nanostructure samples were characterized structurally with scanning electron microscopy (Nova NanoSEM 630,

FEI, Hillsboro, OR) equipped with a Helix detector and with atomic force microscopy (Bruker Dimension Icon, Billerica, MA) using PeakForce QNM tapping mode and a silicon nitride tip. ImageJ software was used to analyze SEM images.

After nanostructure fabrication and characterization, a 0.5 – 1 μm film of SU-8 2000.5 photoresist was deposited onto the samples by spin coating. Samples were soft baked for 1 min at 65 ºC and 1 min at 95 ºC. Photoresist-coated substrates were exposed for 10 seconds with incident powers ranging from 13 to 87 mW with a Ti:Sapphire laser (pulse width τ = 30 fs, repetition rate f = 86 MHz, wavelength $\lambda_{incident}$ = 800 nm) selectively polarized along the short axis or long axis of the nanocrescents. Following exposure, samples were baked for 1 min at 65 ºC and 1 min at 95 ºC, and developed in SU-8 developer for 45 seconds. Finally, samples were rinsed with isopropanol and hard baked for 2 min at 150 ºC. Regions of polymerized photoresist were imaged with SEM and AFM.

3.3 Results and Discussion

We used NTL to fabricate gold nanocrescents to exhibit short- and long- axis dipole plasmon resonances around 800 nm to overlap with the Ti:Sapphire laser used to expose the photoresist. Figure 3.1 shows examples of the physical structure and optical properties of nanocrescents used in the photopolymerization experiment. The gold nanocrescents were characterized with AFM and SEM with representative images shown in Figure 3.1A and B, respectively. Extinction spectra were collected for bare nanocrescents as well as nanocrescents covered by a film of SU-8 photoresist. Figure 3.1C presents extinction spectra for the batch of nanocrescents represented by the

structural characterization data (SEM and AFM images). As expected, the plasmon resonance peaks are red-shifted for photoresist-covered nanocrescents compared to bare nanocrescents. For nanocrescents covered in photoresist, the short axis dipole resonance is observed at 785 nm and the long axis dipole resonance at 995 nm (Figure 3.1C). Additional peaks at 1130 nm (in air) and 1360 nm (in SU-8) are due to closely-spaced, coupled nanocrescents that result from aggregated nanosphere templates. We have observed additional peaks due to coupled structures previously and these peaks are not present in simulations based on a single nanocrescent.

In order to visualize the near-field, we exposed the nanocrescents coated with SU-8 photoresist with a collimated Ti-sapphire laser with a wavelength of 800 nm. This exposing wavelength directly overlaps with the short axis dipole resonance and as a result we expected to observe photopolymerization due to enhanced local fields leading to multi-photon absorption. While the exposing wavelength does not directly overlap with long axis dipole resonance, we probed whether there is enough interaction of the plasmon resonance mode with the incident 800 nm light to enhance multiphoton absorption. We used SEM to image the location of the photopolymerized photoresist regions after developing the photoresist and rinsing away the unpolymerized monomer. The incident power of the laser used to expose the photoresist had to be adjusted. At high incident powers (30 – 90 mW) polymerized photoresist was not localized to individual nanocrescents, but rather was observed as large circle of photoresist that covered both nanocrescents and the underlying substrate. The diameter of the circle corresponded to the diameter of the incident laser beam (30 – 50 μm) and served to inform us of the shape and quality of our exposing source. However, around the edges of the large polymerized

spot, localized photoresist was observed on individual nanocrescents. This was not surprising due to the Gaussian beam profile. As the incident power was decreased (10 – 30 mW) polymerization of photoresist was observed to be localized to individual nanocrescents at the center of the beam.

After exposing the nanocrescents to the laser light and removing unpolymerized photoresist with a developing solvent, we visualized the polymerized regions with SEM. Figure 3.2A and B show representative SEM images of the photoresist when the exposing source is polarized along short axis of the nanocrescent. SU-8 photoresist is localized mostly to the outer edges of the tips of the nanocrescent. It can be seen in the SEM images that the dimensions of the localized photoresist vary from crescent to crescent, but for all structures the photoresist laterally extends within a range of 60 – 90 nm away from the tips. While the dimensions of the localized photoresist are inhomogeneous, the location of the localized resist is uniform indicating that the near-field distribution is localized mostly to the outer edges of the tips. The irregularity of the photoresist dimensions are possibly due to slight structural variations in individual nanocrescents and indicates that the near-field distribution has a high sensitivity to structural variations.

AFM was also used to map the regions of photopolymerization for light polarized along the short axis of the nanocrescents (Figure 3.2C). AFM analysis of these gold nanocrescents was used to determine the tip height, the vertical height of the nanocrescent at its tips, before (39.5 nm) and after (66.3 nm) photopolymerization. This shows that the localized photoresist is 26.7 nm in height. The topographical information of AFM corresponds to the expected near-field behavior in the vertical direction.

Theoretical modeling also was used to predict the behavior of the near-field and

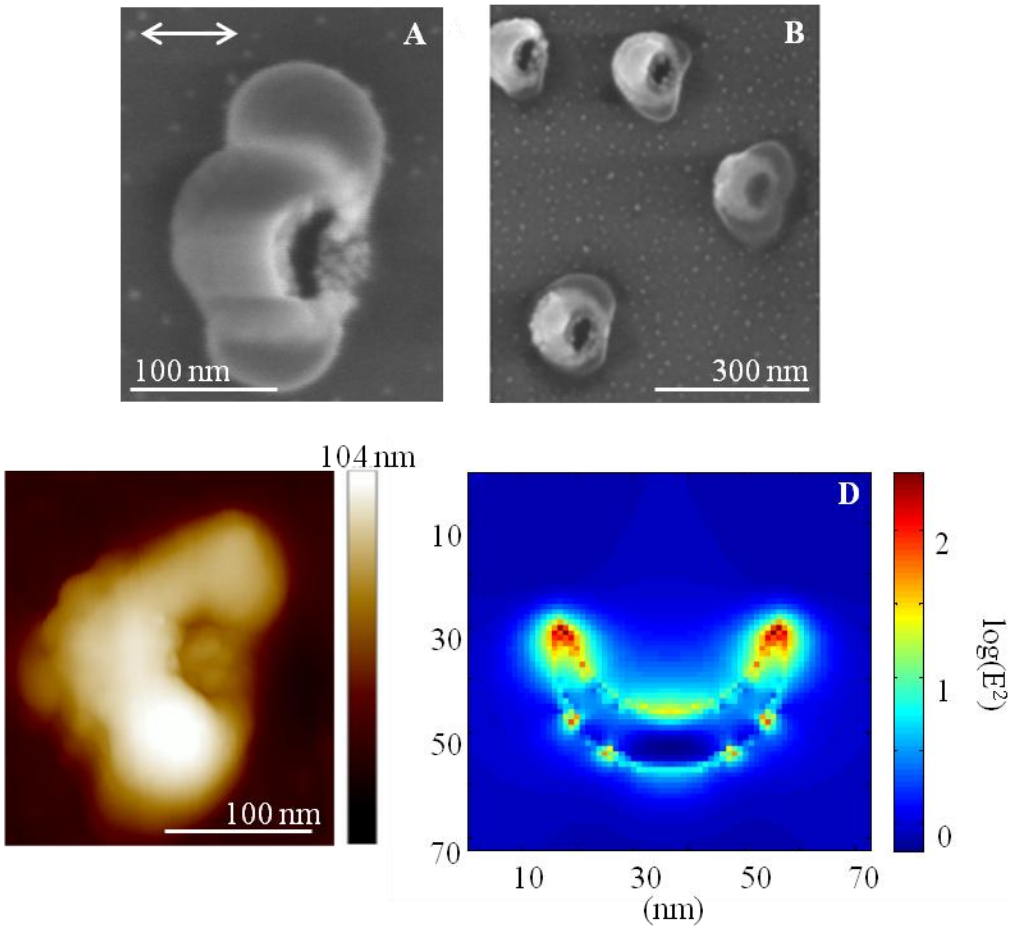

Figure 3.2. Visualization of polymerized photoresist for short-axis polarization. (A) and (B) SEM images of nanocrescents after exposure to the laser and development of the photoresist. The incdent light was polarized as indicated in (A). (C) AFM image of nanocrescent after polymerization of photoresist. (D) FDTD simulation of expected near-field behavior for short-axis polarization for a nanocrescent with dimensions similar to that of the structures used in the photochemical mapping experiments.

to compare to the experimentally mapped near-field distribution for the short axis dipole resonance. Finite difference time domain simulations were carried out with a commercial software package, Lumerical. The simulated nanocrescents were similar to fabricated structures in diameter and height, although the tips of the idealized model nanocrescent were sharper than the tips of the experimentally fabricated structures. The simulated structures were covered with an infinite layer of SU-8 photoresist (refractive index = 1.57 at $\lambda_{incident}$ = 800 nm), and the incident electric field was polarized along the short axis of the nanocrescent structure. Figure 3.2D shows the electric field intensity ($|E|^2$ enhancement) plotted on a log scale. The highest near-field enhancement is localized to the tips of the nanocrescent and extends away from the structure on both sides of each tip. The near-field behavior predicted from simulations strongly correlate with the experimentally mapped fields, which showed photoresist, and thus the near-fields, localized primarily to the outer edges of the tips. The agreement of experiment and theory further supports the localization of the optical near-fields due to the short axis dipole resonance to the tips of nanocrescents.

By rotating the incident electric field polarization to be along the long axis of the nanocrescents, the long axis dipole resonance was selectively excited and its corresponding near-field distribution was mapped through photopolymerization of SU-8 photoresist. Representative SEM images are presented in Figure 3.3A and B. These images show cross-linked photoresist spanning the two tips of the nanocrescents. There is a small amount of material on the outer edges of the tips, but the majority of the photoresist is located between the two tips and spans an area that is several tens of nanometers in width. The location of polymerized photoresist corresponds to the near-

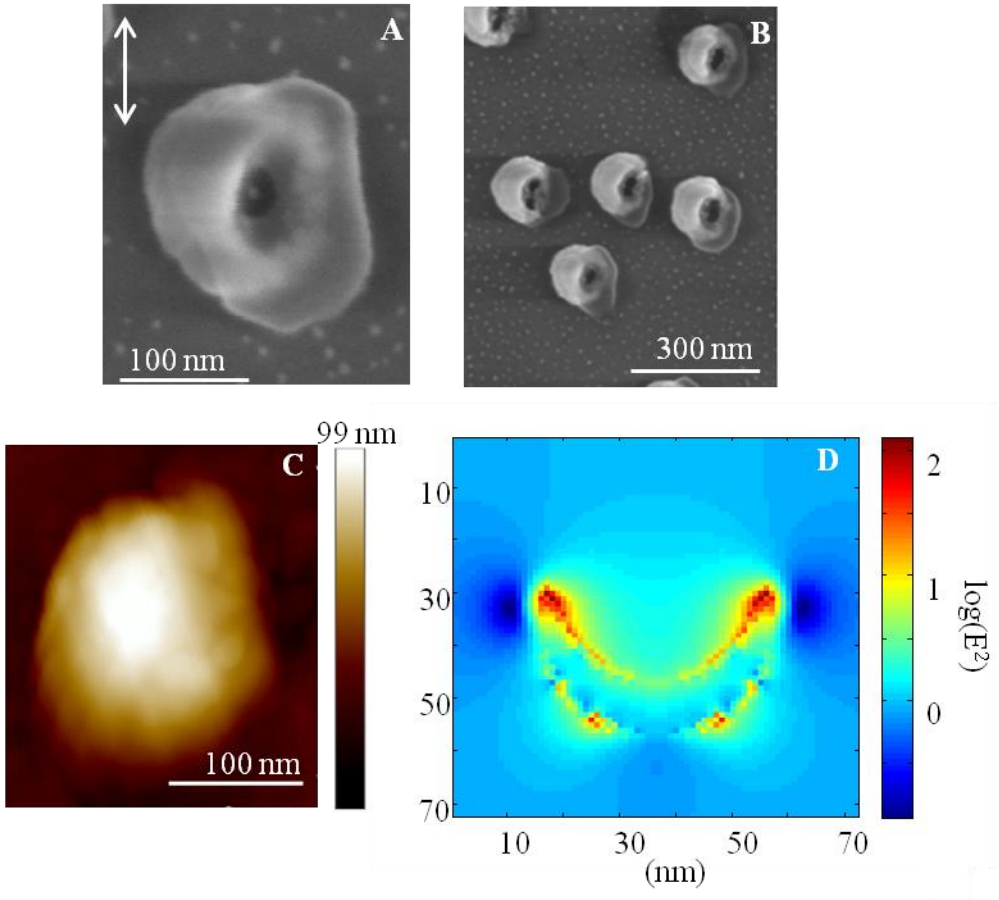

Figure 3.3. Visualization of photopolymerized photoresist for long-axis polarization with incident light polarization indicated by arrow shown in (A). (A) and (B) SEM images and (C) AFM image of nanocrescents after photopolymerization process. (D) FDTD simulation of predicted near-field behavior for a nanocrescent with incident light polarized along the long axis.

field distribution, and indicates that the near-fields induced by the incident light polarization along the long axis of the nanocrescent extend from the tips into the inner diameter of the structure. Unlike the variations in the size of polymerized photoresist observed for the short axis dipole resonance, the polymerized photoresist from the long axis dipole resonance is more uniform in size between structures. This suggests that at the wavelength used to expose the photoresist (800 nm) the near-field distribution from the long axis dipole resonance is less sensitive to variations in nanocrescent structure.

The near-field pattern for long axis polarization also was visualized with AFM (Figure 3.3C) to obtain topographical information about localized polymerized photoresist, and thus the corresponding near-field distribution. While SEM showed photoresist localized between the two tips, the AFM data were less straightforward to interpret with respect to the location of the photoresist, and the structure no longer appears to be crescent-shaped. Resist-mapped nanocrescents appear to be completely covered in photoresist with the tips of the nanocrescent closed up by the material. This may be explained by the variation in height across bare nanocrescents as an artifact of the fabrication process. NTL fabrication causes these nanocrescents to be tallest at the center of the backbone (63.8 nm), with the height tapering down all the way to the tips (39.5 nm). Photoresist locally polymerized due to the enhanced near-field induced by the long axis dipole resonance increases the height of the backbone to 69.5 nm and tips to 51.2 nm, corresponding to a change in height of 5.6 nm and 11.7 nm, respectively. This indicates that the near-fields are enhanced between the tips and along the backbone, with a more intense enhancement in the region spanning the two tips.

The experimental maps of the long axis near-field distribution were compared to theoretical modeling, as described above for the short axis. These simulations varied only in the polarization of the incident electric field and are shown in Figure 3.3D. The highest field enhancement is localized to the inner edge of the tips and extends into the region between the two tips. The simulated optical near-fields are highly comparable to the experimentally mapped fields, indicating that the fields are localized to the inside of the tips and extend into the inner diameter of the crescent. The near-field mapping for both the short and long axis dipole modes shows that plasmonic nanocrescents act as optical antennas to focus light to subwavelength volumes where the location and distribution of confined light can be selectively tuned through incident polarization.

In the system used here, polymerization of SU-8 photoresist by 800 nm light only occurs when plasmonic nanostructures are present and in near-resonance with the exposing wavelength. SU-8 photoresist was spin coated onto substrates that had no enhancing nanostructures, and the photoresist film was exposed to 800 nm light. Regardless of input power, the Ti:Sapphire laser used in these experiments was not intense enough to polymerize SU-8 photoresist on bare glass through multiphoton absorption at 800 nm (data not shown). This indicates that plasmon-induced near-field enhancement is necessary to polymerize SU-8 through multiphoton absorption. Similarly, polymerization does not occur when the incident wavelength is not in resonance with the nanocrescents. Larger (diameter = 535 nm) nanocrescents were fabricated to exhibit a short axis dipole resonance at 1730 nm and long axis dipole resonance that was beyond 3200 nm and could not be measured with the spectrophotometer; both resonances were lower in energy than the exposing wavelength and did not overlap with the 800 nm

exposing light. These nanocrescents were coated with an SU-8 film and exposed with 800 nm light, but no polymerization of the photoresist was observed (data not shown). Lack of polymerization is a consequence of both dipole resonance modes being lower in energy than the exposing wavelength, resulting in no enhancement of the multiphoton absorption process. Localized polymerization, and thus mapping of the near-field distributions, was only observed when plasmon resonances of the nanocrescents were on resonance (or at least overlapping with the tail of the resonance in the case of the long-axis dipole) with the incident light wavelength to enhance multiphoton absorption.

The tunable polarization-dependent near-field distribution and charge oscillation patterns of nanocrescents discussed thus far arise from the structural anisotropy. Symmetric structures like disks[35] or rings[36] have a single, polarization-independent (degenerate) resonance mode, thus the near-field distribution should not be tunable. To compare the near-field behavior of symmetric structures with the asymmetric nanocrescents, gold nanodisks and nanorings were fabricated through variations of nanosphere lithography, and engineered so that their resonance wavelengths overlapped with the excitation at 800 nm. Photochemical mapping with SU-8 photoresist was performed on these structures with the incident laser polarized either vertically or horizontally. Figure 3.4A shows the extinction spectra of gold nanodisks in air and coated with a film of SU-8. A single degenerate resonance mode in air is observed at 775 nm, but when coated in a film of SU-8 photoresist, the resonance wavelength red-shifts to 800 nm which directly overlaps with the exposing wavelength. The nanodisks also were characterized with SEM prior to photochemical mapping (Figure 3.4B); however, no

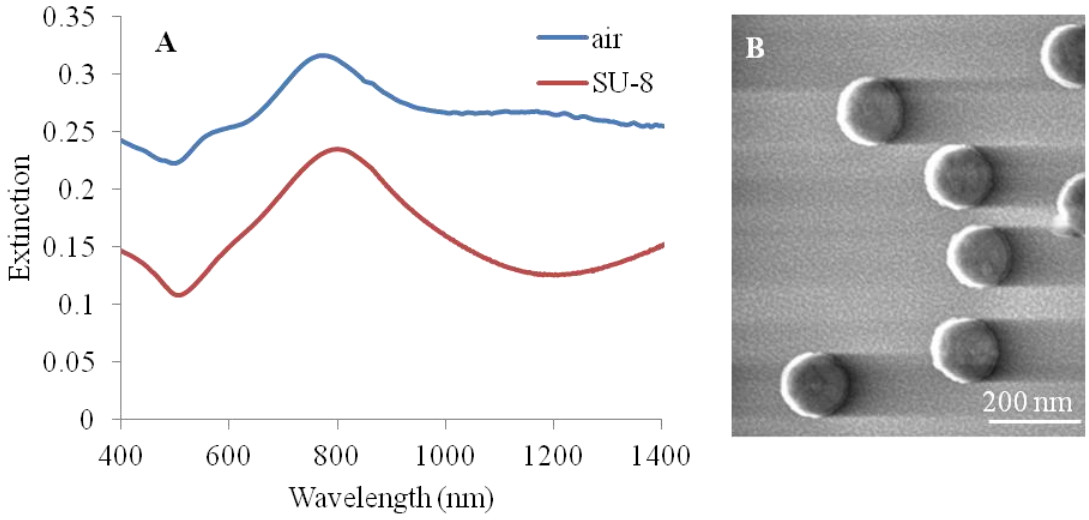

Figure 3.4. Characterization of gold nanodisks. (A) extinction spectra of bare gold nanodisks in air and covered by a film of photoresist. (B) SEM image of bare gold nanodisks before photochemical mapping.

polymerization of the photoresist on the disks was observed with either SEM or AFM (data not shown). This suggests that the dimensions of the polymerized regions are smaller than these techniques can resolve or that the near-fields of the nanodisks were not intense enough to enhance multiphoton absorption by the photoresist.

The near-field distribution of gold nanorings with a degenerate polarization-independent, plasmon resonance mode also was mapped. Figure 3.5A shows the extinction spectra of the nanorings in air and covered by SU-8 photoresist. In air the nanorings are resonant at 1375 nm and in SU-8 the resonance wavelength red-shifts to 1480 nm. While the resonance wavelength did not directly overlap with the exposing wavelength, photochemical mapping of the nanorings showed small regions of locally polymerized photoresist. SEM images of gold nanorings before (Figure 3.5B) and after (3.5C-F) mapping show that the nanostructure is symmetric. Figure 3.5C and D are SEM images of the near-field distribution mapped in photoresist. Polymerized photoresist can be seen on the inner and outer diameter of the ring along the axis of polarization. Exposing light polarized horizontally (Figure 3.5C) leads to photoresist localized on the horizontal axis. Similarly, vertically polarized light results in photoresist localized vertically (Figure 3.5D). For both polarizations, the photoresist domains laterally extend only 10 – 20 nm, which is comparable to the near-field dimensions expected based on measurements of the LSPR wavelength response of nanorings to adsorbed layers by Sutherland et al.[26] Unfortunately, as SEM images were acquired, the electron beam ablated the nanometer sized photoresist regions, making visualization of these regions a challenge. In order to more readily show the photoresist regions, nanorings were overexposed during polymerization, leading to larger regions of photoresist that were

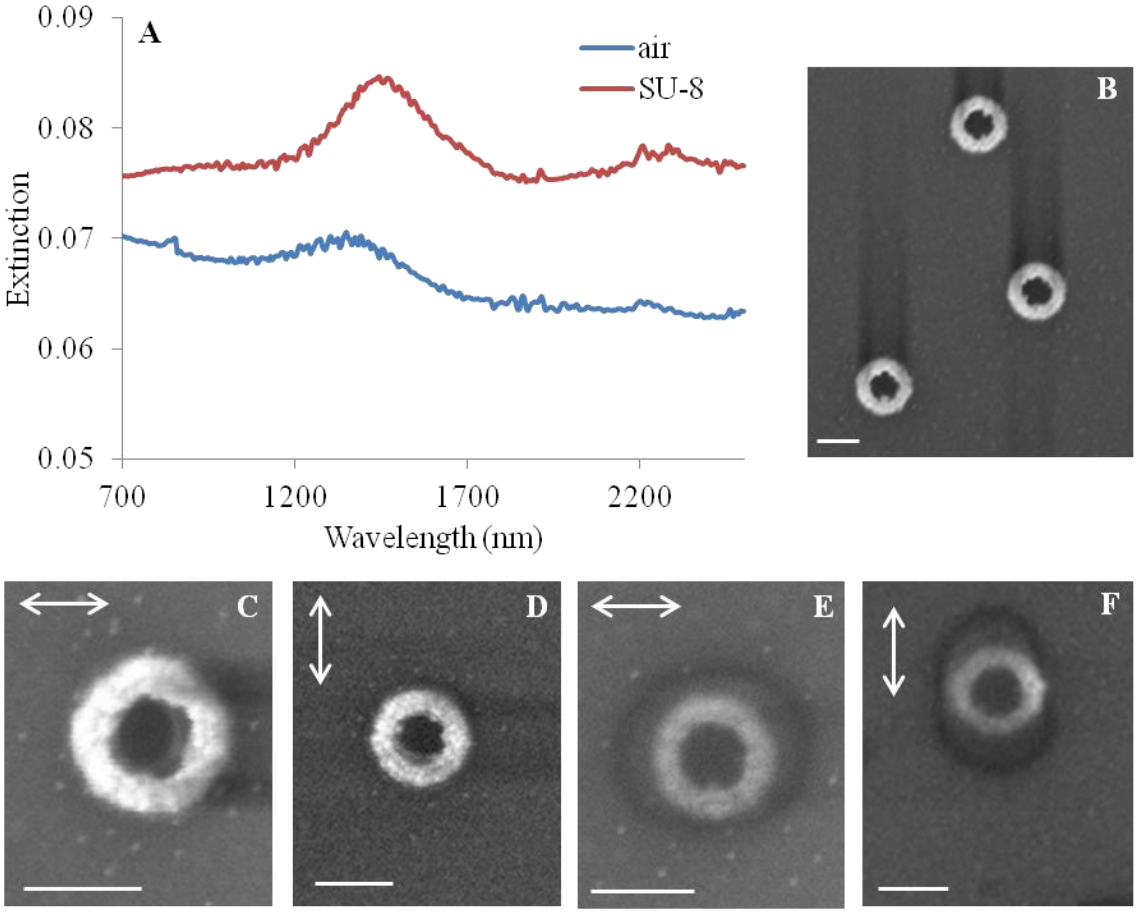

Figure 3.5. Characterization and photochemical mapping of nanorings. (A) LSPR spectra of gold nanorings in an air and SU-8 environment . (B) SEM image of bare gold nanorings. (C-F) SEM images of gold nanorings after photopolymerization. The rings shown in (C) and (D) were exposed to lower laser power, the same power used in the photochemical mapping experiments with nanocrescents. SEM images in (E) and (F) are of rings that were overexposed (i.e., higher laser power used) during photochemical mapping experiments. Incident light polarization with respect to the ring is indicated by the arrow in each image. All scale bars are 100 nm.

more robust in the electron beam. Under the conditions of overexposure of the photoresist, the polymerized region is no longer localized and instead covers the entire structure. The polymerized photoresist extends further away from the ring along the axis of incident light polarization (Figure 3.5E and F). All photochemically mapped rings show that, while the near-field location can be controlled with polarization, the near-field distribution is polarization-independent due to the single electron oscillation pattern that arises from nanorings being structurally symmetric.

All three geometries of nanostructures studied here were comparable in size, composition, and plasmon resonance wavelength. The results show that the dimensions of polymerized photoresist and, thus, the near-field enhancement are dependent on the geometry of the nanostructure. When exposed with the same incident power, regions of localized photoresist on crescents were larger than regions on rings, while no polymerization was observed for nanodisks. The variations in photoresist dimensions between the three types of structures indicate dissimilarity in the intensity of the near-fields of these structures. SEM images of the photochemical mapping show increases in photoresist dimensions, which points to an increased near-field intensity for geometrically asymmetric structures. These results show that the near-fields of nanodisks are the weakest studied here, while the enhanced fields of nanorings are intermediate in strength. Nanocrescents have the most intense near-fields, as evidenced by the larger regions of localized photoresist. These qualitative results correlate well with reported literature values for the local refractive index sensitivity of these structures. While an ensemble value, local refractive index sensitivity is an indication of the intensity of the plasmon-induced near-fields. Disks have a lower sensitivity (60 nm/RIU)[35] than rings

(520 nm/RIU),[26] which also have a lower sensitivity than nanocrescents (440 nm/RIU for the short axis dipole and 880 nm/RIU for the long axis dipole).[21] The correlation between refractive index sensitivity and the magnitude of photoresist indicates that nanocrescent structures act as a better antenna to focus light to subwavelength volumes than either rings or disks.

3.4 Conclusions

In conclusion, the near-field of nanocrescents photochemically mapped through multiphoton absorption of SU-8 photoresist show a tunable near-field distribution that is controlled through incident polarization. The different near-field patterns result from the different plasmon modes that are excited in the asymmetric structure. Symmetric structures, like rings, only have one degenerate resonance mode and correspondingly, the observed near-field pattern did not have a dependence on polarization like the nanocrescents. Nanocrescents, besides having a near-field distribution that can be tailored to specific locations, also have the most intense near-fields of the structures studied here, making them attractive enhancing-substrates for analytical spectroscopies.

3.5 Acknowledgement

This material is based upon work supported by the National Science Foundation under Grant No. DMR 11-21252.

3.6 References

1. Willets, K. A.; Van Duyne, R. P. *Annu. Rev. Phys. Chem.* **2007**, *2007*, 267-297.

2. Atwater, H. *Sci. Am.* **2007**, *296*, 56-63.

3. Rosi, N. L.; Mirkin, C. A. *Chem. Rev.* **2005**, *105*, 1547-1562.

4. Haes, A. J.; Chang, L.; Klein, W. L.; Van Duyne, R. P. *J. Am. Chem. Soc.* **2005**, *127*, 2264-2271.

5. Wu, J.; Chen, F.; Hsiao, Y.; Chien, F.; Chen, P.; Kuo, C.; Huang, M. H.; Hsu, C. *ACS Nano* **2011**, *5*, 959-967.

6. Srituravanich, W.; Fang, N.; Sun, C.; Luo, Q.; Zhang, X. *Nano. Lett.* **2004**, *4*, 1085-1088.

7. Hutter, E.; Fendler, J. H. *Adv. Mater.* **2004**, *16*, 1685-1706.

8. Squalli, O.; Utke, I.; Hoffmann, P.; Marquis-Weible, F. *J. Appl. Phys.* **2002**, *92*, 1078-1083.

9. Campion, A.; Kambhampati, P. *Chem. Soc. Rev.* **1998**, *27*, 241-250.

10. Lakowicz, J. R.; Geddes, C. D.; Gryczynski, I.; Malicka, J.; Gryczynski, Z.; Aslan, K.; Lukomska, J.; Matveeva, E.; Zhang, J.; Badugu, R.; Huang, J. *J. Fluoresc.* **2004**, *14*, 425-441.

11. Kreibig, U.; Genzel, L. *Surf. Sci.* **1985**, *156*, 678-700.

12. Mock, J. J.; Barbic, M.; Smith, D. R.; Schultz, D. A.; Schultz, S. *J. Chem. Phys.* **2002**, *116*, 6755-6759.

13. Chan, G. H.; Zhao, J.; Schatz, G. C.; Van Duyne, R. P. *J. Phys. Chem. C* **2008**, *112*, 13958-13963.

14. Kottman, J. P.; Martin, O. J. F.; Smith, D. R.; Schultz, S. *Chem. Phys. Lett.* **2001**, *341*, 1-6.

15. Hao, E.; Bailey, R. C.; Schatz, G. C.; Hupp, J. T.; Li, S. *Nano. Lett.* **2004**, *4*, 327-330.

16. Klar, T.; Perner, M.; Grosse, S.; von Plessen, G.; Spirkl, W.; Feldmann, J. *Phys. Rev. Lett.* **1998**, *80*, 4249-4252.

17. Hao, E.; Schatz, G. C. *J. Chem. Phys.* **2004**, *120*, 357-366.

18. Chen, C. K.; de Castro, A. R. B.; Shen, Y. R. *Phys. Rev. Lett.* **1981**, *46*, 145-148.

19. Glass, A. M.; Wokaun, A.; Heritage, J. P.; Bergman, J. G.; Liao, P. F.; Olson, D. H. *Phys. Rev. B* **1981**, *24*, 4906-4909.

20. Shumaker-Parry, J. S.; Rochholz, H.; Kreiter, M. *Adv. Mater.* **2005**, *17*, 2131-2134.

21. Bukasov, R.; Shumaker-Parry, J. S. *Nano. Lett.* **2007**, *7*, 113-118.

22. Bukasov, R.; Shumaker-Parry, J. S. *Anal. Chem.* **2009**, *81*, 4531-4535.

23. Bukasov, R.; Ali, T. A.; Nordlander, P.; Shumaker-Parry, J. S. *ACS Nano* **2010**, *4*, 6639-6650.

24. Cooper, C. T.; Shumaker-Parry, J. S. in preparation

25. Haes, A. J.; Zou, S. L.; Schatz, G. C.; Van Duyne, R. P. *J. Phys. Chem. B* **2004**, *108*, 109-116.

26. Larsson, E. M.; Alegret, J.; Kall, M.; Sutherland, D. S. *Nano. Lett.* **2007**, *7*, 1256-1263.

27. Hillenbrand, R.; Keilmann, F. *App. Phys. Lett.* **2002**, *80*, 25-27.

28. Quidant, R.; Badenes, G.; Cheylan, S.; Alcubilla, R.; Weeber, J.; Girard, C. *Opt. Express* **2004**, *12*, 282-287.

29. Hillenbrand, R.; Keilmann, F.; Hanarp, P.; Sutherland, D. S.; Aizpurua, J. *App. Phys. Lett.* **2003**, *83*, 368-370.

30. Amarie, D.; Rawlinson, N. D.; Schaich, W. L.; Dragnea, B.; Jacobson, S. C. *Nano. Lett.* **2005**, *5*, 1227-1230.

31. Hubert, C.; Rumyantseva, A.; Lerondel, G.; Grand, J.; Kostcheev, S.; Billot, L.; Vial, A.; Bachelot, R.; Royer, P.; Chang, S.; Gray, S. K.; Wiederrecht, G. P.; Schatz, G. C. *Nano. Lett.* **2005**, *5*, 615-619.

32. Ueno, K.; Juodkazis, S.; Shibuya, T.; Mizeikis, V.; Yokota, Y.; Misawa, H. *J. Phys. Chem. C* **2009**, *113*, 11720-11724.

33. Sundaramurthy, A.; Schuck, P. J.; Conley, N. R.; Fromm, D. P.; Kino, G. S.; Moerner, W. E. *Nano. Lett.* **2006**, *6*, 355-360.

34. Wenseleers, W.; Stellacci, F.; Meyer-Friedrichsen, T.; Mangel, T.; Bauer, C.; Pond, S. J. K.; Marder, S. R.; Perry, J. W. *J. Phys. Chem. B* **2002**, *106*, 6853-6863.

35. Hanarp, P.; Kall, M.; Sutherland, D. S. *J. Phys. Chem. B* **2003**, *107*, 5768-5772.

36. Aizpurua, J.; Hanarp, P.; Sutherland, D. S.; Kall, M.; Bryant, G. W.; Garcia de Abajo, F. J. *Phys. Rev. Lett.* **2003**, *90*, 057401.

CHAPTER 4

CONCLUSIONS

The nanocrescent is a uniquely tunable plasmonic nanostructure with interesting optical properties. Due to the asymmetry of the structure, several resonance modes, spanning the visible to mid-infrared spectral regions, can be selectively excited by controlling the polarization of the incident light. The two main features of LSPR, resonance wavelength and near-field distribution, were investigated for plasmonic nanocrescents in this work. First, the plasmon resonance wavelength dependence on nanocrescent structural details, such as backbone width, arrayed assemblies, and size, was investigated, followed by a study of the polarization-dependent near-field distribution.

Nanocrescents are fabricated with nanosphere template lithography (NTL) which is a versatile process that allows for several physical parameters to be controlled leading to highly tunable plasmon resonances. Several structural details were investigated systematically to determine their effect on the LSPR properties. UV-visible spectroscopy was used to monitor the changes in LSPR behavior based on shifts in the plasmon resonance wavelengths for the short and long axis dipole resonance modes. The first physical parameter studied was the nanocrescent backbone width, which was controlled

by varying the angle of metal deposition during the fabrication process. Results showed that as the backbone width increased both the short and long axis dipole resonances shifted to shorter wavelengths. These results are promising for tuning the resonance wavelengths to higher energies for applications such as surface-enhanced fluorescence or Raman scattering spectroscopy.

LSPR coupling between adjacent nanocrescents was another parameter that was investigated. The optical response of nanocrescent arrays were compared to those of dispersed, isolated nanocrescents of similar size and composition. A red-shift of the resonance wavelengths for both the short and long axis dipole resonance modes was observed, possibly indicating coupling of the near-fields of adjacent nanocrescents; however, no definitive conclusions can be made about resonance wavelength tunability due to the interplay of several physical factors, such as array orientation, backbone thickness, and tip sharpness, that were unaccounted for.

Various template materials were also investigated for the fabrication of sub-150 nm nanocrescents. Several potential applications of plasmonic nanocrescents require plasmon resonance wavelengths in the visible to near-infrared spectral regions, which necessitates the use of a template with a diameter of 100 nm or less. Polystyrene and silica nanospheres were utilized as templates to fabricate nanocrescents that had plasmon resonances around 800 nm. It was observed that sub-100 nm polystyrene nanospheres melt and are subsequently etched during the metal etching step of the fabrication process, leading to nonideal nanocrescent structures. When sub-100 nm silica nanospheres were employed as the template, it was observed that it was challenging to remove the spheres from the substrate after the fabrication process was complete. Some success in the

fabrication of visible and near-infrared resonant nanocrescents has been shown despite the challenges and limitations of the template materials.

Finally, the polarization-dependent near-field distribution of plasmonic nanocrescents was probed by photopolymerization mapping. Two-photon absorption of photoresist led to selective polymerization in regions of highest near-field enhancement. Due to the asymmetry of the nanocrescent structure, multiple tunable near-field patterns were observed. The short axis dipole resonance led to a near-field pattern where light was localized to the outer edges of the nanocrescent tips, and the long axis dipole resonance had a corresponding near-field pattern that spanned the regions between the two tips of the nanocrescent. These results demonstrated that by controlling the polarization of the incident light, the location and distribution of the near-fields can be selectively tailored.

Overall, plasmonic nanocrescents exhibit a myriad of variable structural details which lead to highly tunable resonance wavelengths that span the visible to mid-infrared spectral regions. The near-field distribution is also tunable through polarization control, resulting in multiple near-field patterns. The tunability in both of these features demonstrates that the nanocrescent in a highly unique structure that can be utilized as a versatile substrate for surface-enhanced spectroscopies.